Mining of alluvial cassiterite and its compositional diversity at the Mayo Darlé area, northern Cameron

Nwamba Maurice Njiganga (mauricenwamba@yahoo.com)
University of Buea
Tebogo Kelepile Tebogo
Ralain Bryan Ngatcha
Cheo Emmanuel Suh
University of Buea
Charles Dieudonne Isiodore Ilouga
Elisha Mutum Shemang
Bih Solange Tantoh
Ernest Tata Tata
Christopher M. Agyingi
University of Buea

Research Article

Keywords: Alluvial cassiterite, EMPA, cassiterite composition, Mayo Darlé area, northern Cameroon

Posted Date: February 23rd, 2023

DOI: https://doi.org/10.21203/rs.3.rs-2612234/v1

Additional Declarations: No competing interests reported.

Version of Record: A version of this preprint was published at Journal of Sedimentary Environments on May 14th, 2023. See the published version at https://doi.org/10.1007/s43217-023-00136-8.

Abstract

Cassiterite mineralization occurs in both the rock and the alluvial system in the Mayo-Darlé area of northern Cameroon. This study focuses on the morphology, mineral inclusions, and composition of alluvial cassiterite derived from Bambol and Mayo Seni localities, where active alluvial mining by artisans constitutes the most important rural economic activity. The cassiterite grains were primarily analyzed by backscattered electron (BSE) images to investigate their morphological characteristics and mineral inclusions. The composition was examined through electron microprobe analysis (EMPA). The cassiterite grains have an irregular to sub-rounded morphology, indicating proximity to the source, although most of the cassiterite grains display evidence of mechanical transport and abrasion. EMPA results show mainly high SnO_2 content (93–103 wt. %), highlighting the predominance of cassiterite minerals in the humid tropical region. Among the Sn substituting elements, only Fe, Ta, and Mn were detected at very low concentrations (Fe = 0.02 to 0.3 FeO, Mn = 0 to 0.04 MnO, and Ta = 0 to 0.2 Ta_2O_5) all in wt. % respectively, suggesting little variation in the alluvial cassiterite compositions. This high SnO_2 content indicates the purity of cassiterite in the area. Binary plots of compositional variation have similar trends, suggesting that cassiterite was derived from a single bedrock source, despite having a mixed signature of pegmatite- and hydrothermal-derived cassiterite. Mineral inclusions include quartz, hematite, and columbite group minerals (CGMs), which were similar in all the samples, suggesting a homogeneous source. The quartz inclusions highlight quartz veins associated with the mineralization and potential felsic plutonic bedrocks. The chemical signatures of the studied cassiterite grains are useful tools to explore the environment of an unknown primary source that can greatly help in mineral exploration in northern Cameroon.

1.0. Introduction

Cassiterite (SnO2) is a common source of tin and is extracted from primary deposits or placer deposits associated with granitic rocks, such as granites and their volcanic and subvolcanic equivalents (Linnen et al., 2012; Tchunte et al., 2021; Konopelko et al., 2022). More than 99% of cassiterite production is from primary and placer ore deposits, with only a very small percentage recovered as a by-product from base-metal mining (USGS, 2020). Cassiterite predominates in active continental margins due to the short survival time of shallow rocks in uplift regions that are prone to weathering and erosion. Hence primary Sn deposits are generally preserved only as relics in placer deposits (Lehmann, 2020).

Placer deposits such as alluvial cassiterite in surface sediments are products of the disintegration of ore bodies and rocks and are relevant to wider cassiterite exploration efforts (Sinclair et al., 2014). Visual confirmation of the presence of alluvial cassiterite focuses interest and allows immediate follow-up panning and prospecting. This can occasionally lead to the discovery of nearby in situ cassiterite mineralization, but the bedrock source is often hidden due to poor exposure. The high mechanical and chemical resistance and stability of cassiterite during weathering, transportation, and accumulation make cassiterite an important tool for source-rock characterization in provenance studies (Fletcher and Loh, 1996a; Romer and Kroner, 2015; Zack and Gahtani, 2015; Edima et al., 2022). Parameters such as transport, deposition, and diagenesis can physically modify cassiterite grains (usually abraded, rounded, and flattened). During transport, the morphology of alluvial cassiterite grains can provide a vector to the location of bedrock sources, while mineral inclusions within the cassiterite grains reflect the mineralogy of the cassiterite primary source (Morton and Hallsworth, 1999). The inclusions can also be used to deduce the chemical conditions of the mineralizing environment (Moles and Chapman, 2011).

Alluvial sediments are commonly composed of quartz, feldspars, and mica as major constituents and a minor amount of heavy minerals such as cassiterite, gold, iron, zircon, rutile, tourmaline, garnet, epidote, chromium spinel, and fluorine-bearing minerals (Meinhold et al., 2008; Lehmann, 2020). Some of these heavy minerals, such as gold, cassiterite, and rutile, are known to constitute valuable ores (Dewaele et al., 2013; Embui et al., 2013; Nyobe et al., 2018; Makshakov and Kravtsova, 2021), especially in the warm, humid climatic and periglacial conditions which are conducive for their liberation from weathered host rocks (Ahmad et al., 2014; Silva et al., 2014; Kermani et al., 2016; Ekoa et al., 2018) and their presence in an area prompts further investigation.

Cassiterite occurrences are reported worldwide, especially in areas of thickened continental crust or within intra-cratonic settings (Linnen, 1998). The African continent is richly endowed with these rare-metal-hosting granites that are linked to orogenic belts such as the Central African Fold Belt (CAFB, Fig. 1a; Melcher et al., 2015).. This fold belt extends from the Gulf of Guinea through Cameroon, Nigeria, and the Cantral African Republic (C.A.R) into Sudan, making these countries suitable hosts for cassiterite mineralization. These countries have witnessed significant attention in recent decades due to an upsurge in the demand for Sn worldwide owing to its wide range of applications in the electronics industries for the production of LED screens, solar cells, iron or steel plating, and superconducting magnets (Girei et al., 2019; Lehmann, 2020; Oyediran et al., 2020). However, cassiterite mineralization, particularly in Cameroon, remains unexplored.

In Cameroon, alluvial cassiterite exploitation started in the early 1930s and continues to date, although it is not well documented in scientific literature despite the growing interest in cassiterite exploration among both smallscale exploration companies and artisanal miners. This commodity is still only reported in the north of the country. In the Mayo Darlé area, cassiterite mineralization occurs as porphyry-type stockwork veinlets with grades up to 0.3% SnO_2 and as vertical and horizontal high-grade (2–20% SnO_2) greisen veins within host alkali biotite granites (Nguene, 1982). In the Mayo Salah area, cassiterite occurs alongside coltan, wolframite, rutile, and pyrochlore as homogeneously disseminated accessory mineral phases in peraluminous muscovite leucogranites (Tchunte et al., 2018). Despite these efforts, geochemical signatures associated with such cassiterite occurrences that could contribute to our understanding of the mineralization in the region remain uninvestigated.

In an attempt to discover new cassiterite potentials in the northern part of the country, we launched a stream sediment survey targeting the Mayo Darlé area drainage system. The current study presents the first alluvial cassiterite data for the Mayo Darlé area. We report in this paper the morphological, mineralogical, and chemical features of alluvial cassiterite grains from the Bambol and Mayo Seni localities. Granitic rocks underlie most of the catchment as outcrops, and we speculate that a cassiterite-bearing granitic system is the principal controlling factor.

2.0. Geological Setting

2.1. Regional Geology

The evolution of the Neoproterozoic Central Africa fold belt (CAFB, Fig. 1a) can be attributed to the convergence and collision between the São Francisco-Congo Craton to the south, the West African Craton (WAC) to the west, the Sahara metacraton, and a Pan African Mobile Belt (Abdelsalam et al., 2002; Toteu et al., 2006; Ngako et al., 2008; Van Schmus et al., 2008; Li et al., 2017). The CAFB underlies parts of Cameroon, Chad, and the Central African Republic, between the Congo Craton to the south and the Western Nigeria shield to the north, and extends eastward to Sudan and Uganda (Li et al., 2017). The tectonic evolution of the CAFB in central and southern Cameroon resulted in structures including a N70^{o}E sinistral shear zone in central Cameroon known as the Central Cameroon Shear Zone (CCSZ) (Fig. 1b). Several subsidiary NE-trending shear zones splay off the main shear zone (Central Africa Shear Zone (CASZ)), including the Tcholire Banyo shear zone (TBSZ) to the north and an E-W Sanaga shear zone (SSZ) to the south with a N300E to N700E orientation (Fig. 2b; Ngako et al., 2003, 2008: Suh et al., 2006; Tchameni et al 2006). Petrologic and isotopic data collected along these major shear zones in Cameroon have been used to subdivide this mobile belt in Cameroon into the following lithotectonic domains: (1) the Yaoundé Domain (YD), (2) the Adamawa-Yadé Domain (AYD), and (3) the North Western Cameroon Domain (NWCD), to which the present study area belongs (Fig. 1b, Toteu et al., 2004; Kankeu et al., 2009; Ngoniri et al., 2021).

The Mayo Darlé area is part of the North Western Cameroon Domain (NWCD). This domain includes: (1) Neoproterozoic medium- to high-grade schists and gneisses (of volcanic and volcano-sedimentary origin composed of sodic rhyolite, tholeiitic basalts, and variably reworked clastic rocks or purely volcanogenic clastic rocks represented by the Poli series); (2) Pan-African pre-, syn-, and late-tectonic granitoids (diorites, granodiorites, and granites) mainly of calk-alkaline composition emplaced between 660 and 580 Ma; and (3) post-tectonic alkaline granitoids with mafic to felsic dykes (Toteu et al., 2001, 2006; Tchunte et al., 2018). Numerous basins with unmetamorphosed sedimentary and volcanic rocks, corresponding to molassic deposits of the Pan-African orogeny, are equally reported (Montes-Lauar et al., 1997). This domain is distinguished by lower Palaeoproterozoic crust contributions in Pan-African plutonic rocks, implying a discontinuous to absent Palaeoproterooic basemeznt (van Schmus et al., 2008). Palaeoproterozoic inheritance (1.5–2.1 Ga; Ferré et al., 1998, 2002) is more important in the tin metallogenic province (~ 560 Ma; Woakes et al., 1987) of Eastern Nigeria. It is not yet clear whether or not the Eastern Nigeria terrane (ENT) belongs to a different block and is separated from the NWCD by a major crustal boundary. However, based on the presence of post-collisional granites (627 Ma) and distinct isotopic signatures of ENT compared to the NWCD granitoids, they may have undergone different Pan-African evolutions before the final amalgamation of the terranes sandwiched between the Sahara metacraton and the Congo craton of west Gondwana (Bute et al., 2019). Three deformation episodes are described in the NWCD. Horizontal foliations (D1) are defined by folds with SW-NE trending axial planes (D2) and major ductile transcurrent shearing (D3) associated with the Tcholliré Banyo Fault and regarded as conduits and traps for Pan-African crustal scale ore-bearing hydrothermal fluids (Toteu et al., 2006; Tchameni et al., 2013; Houketchang et al., 2015; Ketchaya et al., 2022). Within this domain, the Mayo Darlé plutonic area, the Rey Bouba Greenstone Belt, and the Poli Series are known for hosting significant mineralization of tin, gold, and uranium (Embui et al., 2013; Nguene, 1982; Kouske et al., 2012, www.altusstrategies.com).

2.2 Local geology and petrography

The localities under study occupy the eastern part of the Mayo Darlé area (Fig. 1c), which is composedof basement gneisses and mylonites (with minor occurrences of granulitic metapelites and metabasites), intruded by granitoids and volcanic rocks. The basement complex rocks consist of medium- to coarse-grained amphibole-biotite and garnet-bearing migmatitic gneisses exposed along slopes as slabs (Fig. 2a). The gneisses are weakly foliated, characterized by alternating mafic and felsic bands trending NE-SW, and locally have quartz-filled fractures (Fig. 2b). The basement gneisses tend to be more leucocratic at their contact with the granitoids. The granitoids dominate the area under study and include biotite granite, granite greisens, and granite porphyry. They are largely leucocratic and vary from medium- to coarse-grained with sporadic foliation characterized by felsic (quartz-rich) and mafic (biotite-rich) mineral segregation (Fig. 2c–d). The granitoids have been described in detail by Nguene (1982) as representing part of a regional-scale batholith with stanniferous quartz veins in structurally favorable sites. These ferruginized cassiterite-bearing quartz veins trend NE-SW and are enclosed by hydrothermally altered zones traceable into the wall rock with disseminated cassiterite. This altered host body is characterized by greisenization, sericitization, silicification, kaolinization, and hematization. Together with the mineralized veins, they constitute the main targets for primary cassiterite mining by the local artisans and semi-mechanized enterprises (SME). Rhyolites and rare basalt floats are the main volcanic rocks in the area. The rhyolites are fine-grained and show structural features such as columnar joints, with joint alignment suggesting the direction of flow for the rocks tapering NE-SW (Fig. 2e–f).

Deep valleys and chains of topographic highs up to 2024 m above sea level characterize the terrain, resulting in a dendritic drainage pattern in many parts of the study area (Fig. 3). This dranaige system contributes to the accumulation of heavy minerals such as cassiterite, which are weathered, eroded, and transported from the granitoids. The Bambol and Mayo Seni areas are the main artisanal mining sites for alluvial cassiterite (Fig. 4). These mining sites are about 15 to 25 km away from the exposed primary cassiterite-bearing veins and host rock. The cassiterite grains are variable in size due to mechanical abrasion during transportation. In these areas, artisanal mining activities recover cassiterite using water-powered (hydraulic pump) and sluice box techniques in alluviums.

3.0. Sampling And Analytical Methods

In the field, homogenized samples of sediment were collected from pits on the stream channels along the course of the Bambol and Mayo Seni streams. In order to obtain alluvial cassiterite concentrates by the panning method, sediments from each pit were first weighed, then panned and/or washed using a sluicing box. The heavy mineral concentrate obtained was then further purified using heavy liquid and magnetic separation techniques to isolate the cassiterite grains. Cassisterite grains were then handpicked from this purified heavy mineral fraction under a binocular microscope. These grains were then

mounted in epoxy resin, and the surface was polished in preparation for microanalysis. Prior to the analysis, the representative polished sections were coated with carbon film to achieve surface conductivity. To determine the morphology and other features of the grains, the polished mounts were studied and photographed under reflected and transmitted light and later by backscattered electron (BSE) images.

A total of 265 analyses (major and minor elements) of cassiterite from 9 samples (samples 1B, 2A, 2B, 3A, 3B, 4A, 4B, 5A, and 5B) were carried out using a three-channel JEOL JXA-8230 electron probe microanalyzer (EPMA) at the Botswana International University of Science and Technology (BIUST). The EPMA was set to a 15 kV acceleration voltage, a beam current of 15 nA, and a beam diameter of 2 μm. The following analytical standards and lines were used: orthoclase (Si, K), diopside (Ca, K), magnetite (Fe, K), cassiterite (Sn, L), Ta metal (Ta, M), and rhodonite (Mn, K). Care was taken during EMP-analysis to select analytical points that were free of cracks. The analyzed data were collected with JEOL software, and a ZAF matrix algorithm was used to correct for differential matrix effects. The samples were classified under national standards for natural minerals or synthetic metals, and the implementation standard is GB/T 15074 – 2008 General Rules for Quantitative Analysis of Electronic Probes, with an analytical accuracy of 0.01%.

4.0. Results

4.1. Morphology and surface characterizations of cassiterite grains

The cassiterite grains from the study area display a wide range of shapes and sizes. The grains are medium to coarse and range from 1 mm to ~ 1 cm (Fig. 5a-b). Based on the morphology, three categories of cassiterite grains were identified: (i) angular to sub-angular grains, which make up 80% of the grains; (ii) sub-rounded and rounded to spherical grains, which constitute 15% of the grains; and (iii) 5% slender or elongated grains (Figs. 5, 6, 7, 8, 9, 12, & 13). The angular to sub-angular grains that make up the majority of cassiterite grains, as well as the elongated grains, are generally irregular and anhedral. The sub-rounded and rounded grains have smooth surfaces (Fig. 8), while others have pitted or rough surfaces. Overall, most of the grains show rough and irregular surfaces. In most of the grains, the rims are bent and fractured from rims to cores, while some show folded edges (Fig. 13). Cassiterite grains from the Bambol locality display similar morphologies to those from Mayo Seni. In some cases, the subgrains are detached or dismembered from the parent cassiterite grains (Figs. 8a, c, d, 9d, e, and Figs. 13a, d, e). The cassiterite grains from both localities are zoned. The cassiterite grains from the study area exhibit some microscopic features such as cracks, cavities, and mineral and fluid inclusions (Figs. 5–9), while Figs. 10 and 11 show striations. These cracks, cavities, and striations suggest intensive physical damage resulting principally from hammering and abrasion during fluvial transport. The cavities are irregularly interconnected within the cassiterite grains from rims to cores, but predominantly at the rims of the grains, and are commonly filled by opaque minerals. These microtextures are mainly created by hammering and abrasion.

4.2. Mineral association and inclusions in cassiterite grains

Mineral inclusions embedded in cassiterite grains are very important for the identification of their source. Despite the scarcity of mineral inclusions within cassiterite placers, they were identified in Mayo Darle cassiterite grains, as observed in Figs. 5–13. The cassiterite grains from both localities reveal mineral association and inclusions such as quartz, hematite, and CGM entombed in the grains, occuring either in cavities or as patchy deposits around the rims of the cassiterite grains (Figs. 5–13). The quartz and other inclusions are expressed as interstitial grains and are subhedral to anhedral. The BSE images show that CGM has concordant rim-core normal progressive zoning as stringers (Figs. 8b, 12d, and 13b). We equally distinguished a rarely patchy zoning of CGM in some grains (Figs. 13a, c, d, and e). Zoning is brighter from rim-core in all the grains corresponding to CGM, which constitutes the brightest parts of the cassiterite grains and is consistent with magmatic fractionation in agreement with other worldwide studies. Although grains from both localities have similar mineral associations, inclusions, and features, they differ in that they have fluid inclusions (Figs. 5b and 11a).

4.3 Chemical composition of cassiterite grains (EMPA data)

EMPA data for all 265 analyses performed as well as representative BSE images of cassiterite from alluvial sediments studied are presented in Tables 1–9 and Figs. 5–13. Cassiterite (SnO_2) grains from both localities occur in association with Fe, Si, Ca, Mn, and Ta. Grains from the Bambol locality show Sn contents that vary from 95 to 103 wt % SnO_2, with samples 2A and 4B (Tables 2 and 7) having the highest concentrations, followed by Fe, whose contents reach a maximum of 1 wt. % FeO as detected in some grains. The concentration of Si ranges from 0.2 to 0.3 wt. % SiO_2, while Ca contents vary between 0.6 and 0.7 wt. % CaO. The Mn content ranges from 0.02 to 0.12 wt. % MnO, coupled with Ta contents that vary between 0.03 and 0.29 wt. % (Tables 1, 2, 7, 8, and 9), and the points analyzed are shown in Figs. 5, 6, 11, 12, and 13. Grains from the Mayo Seni locality reveal Sn contents that vary between 91 and 100 wt. % SnO_2 (Tables 3, 4, 5, and 6); the points analyzed are shown in Figs. 7, 8, 9, and 10. Associated elements occur in low quantities: Si (0.2 to 0.3 wt. % of SiO2), Ca (0.6 to 0.8 wt. % of CaO), Mn (0 to 0.05 wt. % of MnO), and Ta (0.02 to 0.2 wt. % of Ta2O5), with the exception of Fe, which shows an elevated concentration that reaches a maximum of 0.9 wt. % of FeO (Tables 3, 4, 5, and 6).. Therefore, Sn contents in both localities are similar, though slightly higher in Bambol than in Mayo Seni. The concentrations of SnO2 in the analyzed points containing CGMs are lower (ranging from 93 to 96 wt. %).

Based on the analyzed points, Sn contents vary from rims to cores, where the cores with analyzed points have higher Sn contents as compared to those of the rims, which is a trend in both localities. Though there are some exceptions where the Sn content is evenly distributed throughout the grains (Table. 1).

5.0. Discussion

5.1. Cassiterite grains morphological characterization as indicators to source- proximity

Alluvial cassiterite grains have been investigated at different locations in the Darlé area. The elevated topographic highs and deep valleys (2024 m, Fig. 3) aided deep weathering, erosion, transport, and deposition in the low-lying Bambol and Mayo Seni localities. Most of the cassiterite grains from these

localities have irregular morphologies (Figs. 5, 7, and 9–13) and these crystal imprints are diagnostic features used to express transport mechanisms as interpreted to represent recently liberated grains from the source rock or suggest a relatively short transport distance (Fletcher and Loh, 1996a; Tchunte et al., 2018; Ngouabe et al., 2022). As the cassiterite grains are progressively transformed in the course of stream transportation, the morphology evolves to be angular and semispherical (e.g., Figs. 5a, 8a, and 8c). The regular and semispherical grain shapes reflect long distances of transport (Tchunte et al., 2018; Ngouabe et al., 2022). The surface texture of the cassiterite grains is subsequently modified or evolves from pitted and rough to smooth (Figs. 8a–c). These features all depend on the stream's energy and sediment composition (Fletcher and Loh, 1996a). In this study, proximity-to-source is evaluated based on the different morphologies presented by the cassiterite grains. According to the morphological features, we categorize the cassiterite grains from both localities into three groups: (i) angular to sub-angular grains; (ii) sub-rounded, rounded to spherical; and (iii) slender or elongated grains (Figs. 5, 6, 7, 8, 9, 12, and 13). During their transport downstream from the supposed sources, the cassiterite grains were exposed to distinct changes. Angular grains depict newly liberated grains from the potential source rock, suggesting a short distance of transport and proximity to the source (Ketchaya et al., 2022; Ngouabe et al., 2022). Despite the short distance of transportation, the morphology of the grains subsequently undergoes modifications from subrounded to round (Fig. 8), resulting from physical hammering and abrasion as the transportation distance increases downstream. As a result, these subrounded to rounded grains imply a distance from the source. This suggests cassiterite grains from this locality have undergone a longer distance of transportation as compared to those from Bambol. Some grains show fragmentation or detachment from the parent cassiterite grains (Figs. 8a, c, d, 9d, e, and Figs. 13a, d, e). These provide evidence for grain size reduction during the course of transportation and the liberation of inclusions and rough edges (Ateh et al., 2021). Despite the fact that cassiterite grains from both localities have similar morphological characteristics, a portion of the grains from Mayo Seni are subrounded to round (Fig. 8). According to Chapman et al. (2002), the occurrence of cavities in the grains is a result of dislodgement or disaggregation of gangue minerals such as quartz due to their hardness and resistance to abrasion during transport, but also of the action of dissolution considering the chemical instability of minerals such as calcite.

5.2. Mineral inclusions within alluvial cassiterite grains

Mineral inclusions in grains have been used to predetermine primary depositional conditions globally (Chapman et al., 2021; Ketchaya et al., 2022). Characterizations of the inclusion suite provide evidence for the mineralogy and thus elucidate the source mineralization type (Chapman et al., 2011). In this study area, mineral inclusions identified are mainly hematite, quartz, and CGM, with hematite inclusions dominating (Figs. 5–13). The cassiterite grains and mineral inclusion populations from the two localities are similar, suggesting derivation from a homogeneous source or mineralization type. Apart from revealing the original host rocks, the mineral inclusions also indicate close proximity to the source, as retaining them in the grains without being leached out or weathered implies a short transportation distance, which is a factor of source proximity. The recurrence of quartz as an inclusion in cassiterite grains from the two localities indicates a link with a mineralized quartz-rich primary source such as greisens, granitoids, and porphyries. "Non-ore" mineral inclusions such as silicates (quartz), according to Chapman et al. (2021), may indicate the lithology of the country rocks. In this study, the inclusion of a "non-ore" mineral is mainly quartz. Hence, the Mayo Darlé area granitoids bearing multiple quartz veins are the potential original source of the mineralization. The study area inclusions (hematite, quartz, and CGM) are similar to silicates and hematite inclusions reported in alluvial gold grains from the Gamba district, northeast of the study area, in the same domain (Ketchaya et al., 2022). In the Mayo Salah area, cassiterite is described to occur in association with coltan, wolframite, pyrochlore, and rutile as homogeneously disseminated grains in muscovite leucogranite (Tchunte et al., 2018). The inclusions of mineral grains such as zircon and albite in the columbite-group minerals (e.g., coltan) reported by the author are equally in favor of a primary source such as greisens, granitoids, or porphyries. Furthermore, uraninite inclusions in pyrochlore minerals that rim Columbite-group minerals, as described by Tchunte et al. (2018), support a granitic origin for the mineralization. Apart from inclusions, the cassiterite grains show core-rim zonation (Figs. 11 and 13), resulting from chemical leaching during fluvial transport (Craw et al., 2015).

5.3. Chemical compositional variations of alluvial cassiterite grains

The analyzed alluvial cassiterite grains from Bambol and Mayo Seni show only little compositional variation, and only a few elements (Si, Ca, Fe, Mn, and Ta) can be identified in addition to Sn. The Sn content reaches a maximum of 103 wt% SnO2 here. This indicates that the cassiterite is quite pure and supports the need for further development of alluvial workings in the area. The cassiterite grains from the two localities have similar Sn concentrations, but the grains from Bambol have slightly higher Sn contents than those from Mayo Seni, and the concentrations are higher in the cores than in the rims. This may be due to some chemical impurities or physical damage at the rims. Moreover, the high Sn content of the grains indicates a magmatic signature of the mineralized fluids for the primary ore in the bedrock (Seranti et al., 2002; Lehmann, 2020; Gemmrich et al., 2021). Such elevated contents of Sn are arguably reflective of highly evolved granites (Pettke et al., 2005). With respect to elements usually substituting for Sn in cassiterite, such as Fe, Nb, Ta, Ti, W, and Mn (Neiva, 1996), the Mayo Darlé area cassiterite grains display low Fe, Ta, and Mn contents, with a negative correlation of SnO_2 with oxides of these elements (Fig. 14). This indicates that the mineralizing fluids were low in Fe-Ta and Mn, which is common in granitic and associated greisens systems (Murciego et al., 1997; Seranti et al., 2002; Dewaele, 2013; 2015; Liorens et al., 2016; Gemmrich et al., 2021). The clustering of the data in Fig. 14 indicates a single bedrock or homogeneous source derivation (Norman and Chapman, 2011).

The low Fe and Mn contents noted in the studied cassiterite samples might be the result of alteration or leaching from the host granitic rocks (Tack et al., 2010; Zhang et al., 2017). Ta is generally mobile under much reduced conditions, and cassiterite is transported in hydrothermal solutions mostly as Sn^{2+} (Seifert et al., 1997). Thus, the presence of Ta in the Mayo Darle cassiterite may suggest that highly reduced fluids transported and deposited the ore mineral. This therefore points to the involvement of a magmatic-hydrothermal fluid component in the formation of the Mayo Darle cassiterite ore. The plot (Fig. 15) of the Mayo Darlé cassiterite grains alongside cassiterite grains from other world-class deposits (e.g., Gejiu Tin District, Yunnan Province, and the Fujian Tin Province), points to a mixed signature (magmatic-hydrothermal). The pegmatite-derived cassiterite field contains the majority of the cassiterite grains from this study plot. Cassiterite data from the Mushiton tin deposits (Konopelko et al., 2022) and the Numbi tin deposits (DRC) are plotted on the hydrothermal cassiterite field.

The formation of CGM in the granite-related system has been extensively associated with magmatic and hydrothermal processes (Belkasmi et al., 2000; Liorens et al., 2016; Lerouge et al., 2017). Tchunte et al. (2018) suggest a two-stage mineralization of columbite in the Mayo Salah area, northern Cameroon, associated with leucogranite emplacement during continental collision tectonics (582 ± 7 to 597 ± 8 Ma, U-Pb dating of monazite). An early Nb-rich Mn-columbite stage related to magmatic fractionation was dated at about 603 ± 5 Ma (U-Pb dating of columbite) and a late Ta-rich Mn-columbite stage related to hydrothermal overprint dated at 588 ± 5 Ma (U-Pb dating of columbite). According to Astrid et al. (2020), the formation of CGM associated with hydrothermal fluid-induced alterations is related to dissolution-reprecipitation processes at the final stage of post-magmatic evolution. The chemical compositional variations of cassiterite grains from granite-related systems probably reflect the complex processes of Sn-ore deposits. CGM, which constitutes the brightest parts of the cassiterite grains, is consistent with magmatic fractionation in agreement with other worldwide studies (Van Lichtervelde et al., 2007).

6.0. Conclusion

Based on the mineralogy and geochemical composition of the alluvial cassiterite concentrates of the Bambol and Mayo Seni localities in the Mayo Darlé region, the following conclusions are derived:

1. The alluvial cassiterite grains range from angular to subangular, generally irregular, subrounded to rounded, and elongated, indicating that they were liberated directly from their source and transported into the fluvial system. Thus, it could serve as a useful guide in the exploration for cassiterite in the bedrock.
2. The presence of quartz in cassiterite grains from the Bambol and Mayo Seni localities suggests a connection to a mineralized, homogeneous quartz-rich primary source, such as greisens, granitoids, and porphyries.
3. The elevated Sn contents (> 98 wt. %) with low concentrations in Si, Fe, Ta, and Mn reflect the purity or high grade of the alluvial cassiterite, suggesting the good economic potential of the alluvial cassiterite concentrates from the Mayo Darlé area.
4. Cassiterite grains from the two localities are clustered together on the discrimination plots, suggesting a single derivation or a homogeneous system.

Declarations

Author Contributions

Conception of the research; CES, CMA and EMS. Field work, laboratory analyses and data synthesis: NMN, TK, IC, CES, EMS, RBN, ET. NMN prepared the first draft of the manuscript. Writing, review, and editing of the manuscript: all authors. Funding Acquisition: CES and EMS

Acknowledgement

This paper is part of the PhD thesis of the first author. The analyses were completed within the cooperation framework between University of Buea and BIUST through CES and EMS. Funding from both institutions is gratefully acknowledged.

References

1. Abdelsalam, M. G., Liegeois, J.P., & STERN, R.J. (2002). The Saharan metacraton. Journal of AfricanEarth Sciences, 31, 119 –136.
2. Ahmad, A.H.M., Noufal, K.N., Masroor, A.M. and Tavheed, K. (2014). Petrography And Geochemistry of Jumara Dome Sediments, Kachchh Basin: Implications for provenance, Tectonic Setting and Weathering Intensity. Chinese Journal of Geochemistry, 33, 9-23. https://doi.org/10.1007/s11631-014-0656-4
3. Armstrong-Altrin, J.S., Machain-Castillo, M.L., Rosale-Hoz, I., Caranza-Edward, A., Sanchez-Cabeza, J.A., Ruiz-Fernandez, A.C. (2015). Provenance and depositional history of continental slope sediment in the southwestern Gulf of Mexico unraveled by geochemical analysis.Cont. shelf Res. 95, 15-26.
4. Astrid, S., Rodolfo, G., & Silvio,R.F.V., (2020). Occurrence and composition of columbite –(Fe) in the reduced A-type Desemborque pluton , Garciosa Province (S-SE Brazil).
5. Ateh, K. I., Suh, C. E., Shuster, J., Shemang, E. M., Vishiti, A., Reith, F., & Southam, G. (2021). Alluvial gold in the Bétaré Oya drainage system, east Cameroon. Journal of Sedimentary Environment, 6, 201–212.
6. Belkasmi , M., Cuney, M., Pollard, P.J., Bastoul, A., (2000). Chemistry of the Ta-Nb-Sn-W oxide minerals from the Yichun rare metal granite (SE China): Genetic implications and comparison with Moroccan and French Hercynian examples. *Mineral .Mag.2000, 64,507-523*.
7. Bute, S.I., Yang, X.-Y., Cao, J., Liu, L., Deng, J.-H., Haruna, I.V., Girei, M.B., Abubakar, U., Akhtar, S. (2019). Origin and tectonic implications of ferroan alkali-calcic granitoids from the Hawal Massif, east eastern Nigeria terrane: clues from geochemistry and zircon U-Pb Hf isotopes. Int. Geol. Rev. https://doi.org/10.1080/ 00206814.2019.1593250.
8. Chapman, R.J., Banks, D.A., Styles, M.T., Walshaw, R.D., Piazolo, S., Morgan, D.J., Grimshaw, M.R., Spence-Jones, C.P., Matthews, T.J., Borovinskaya, O. (2021). Chemical and physical heterogeneity within native gold: implications for the design of gold particle studies. Miner Deposita. https://doi.org/10.1007/s00126-020- 01036-x
9. Chapman, R. J., Mortensen, J. K., & LeBarge, W. (2011). Styles of lode gold mineralization contributing to the placers of the Indian River and Black Hills creek, Yukon territory Territory, Canada as deduced from microchemical characterization of placer gold grains. Mineralum Deposita, 46, 881–903.

10. Craw, D., MacKenzie, D., & Grieve, P. (2015). Supergene gold mobility in orogenic golddeposits, Otago Schist, New Zealand. New Zealand Journal of Geology and Geophysis, 58, 123–136.
11. Dewaele., S N. Hulsbosch, N., Y. Cryns, Y.,Boycec, R. Burgessd, Ph. Muchez, P.H. (2015). Geological setting and timing of the world-class Sn, Nb–Ta and Li mineralization of Manono-Kitotolo (Katanga, Democratic Republic of Congo). http://dx.doi.org/10.1016/j.oregeorev.2015.07.004 0169-1368.
12. Dewaele, S., Goethals, H., & Tom, T.T. (2013). Mineralogical characterization of cassiterite concentrates from quartz vein and pegmatite mineralization of the Karagwe-Ankole and Kibara Belts, Central Africa. GEOLOGICA BELGICA, 16/1-2: 66-75.
13. Edima Yana, R.W., Ondoa, A.D.B., Atouba, L.C.O., Fagny, M.A.,Bessa, A.Z.E. and Faarouk, N.O. (2022). Mining Implication in the Geochemical Exploration of Fluvial Sediments of the East Nyambaka Volcanic Zone (Adamawa-Cameroon). International Journal of Geosciences, 13, 361-381. https://doi.org/10.4236/ijg.2022.135020.
14. Ekoa Bessa, A.Z., Ngueutchoua, G. and Ndjigui, P.D. (2018). Mineralogy and Geochemistry of Sediments from Simbock Lake, Yaoundé Area (Southern Cameroon): Provenance and Environmental Implications. Arabian Journal of Geosciences, 11, Article No. 710. https://doi.org/10.1007/s12517-018-4061-x
15. Embui, V. F., Omang, B. O., Che, V. B., Nforba, M. T., Suh, E. C. (2013). Gold grade variation and stream sediment geochemistry of the the Vaimba-Lidi drainage system, northern Cameroon. Natural Science, 5(2A), 282–290.
16. Ferre, E.C, Gleizes, G., & Caby, R. (2002). Obliquely convergent tectonics and granite emplacement in the Trans-Saharan belt of Eastern Nigeria. Synthesis: Precambrian Res. 114, 199–219.
17. Ferre, E.C., Caby, R., Peucat, J.J., Capdevila, R., Moni´e, P. (1998). Pan-African, post- collisional, ferro-potassic granite and quartz-monzonite plutons of Eastern Nigeria. Lithos 45, 255–279. https://doi.org/10.1016/S0024-4937(98)00035-8.
18. Fletcher, W.K., & Loh, C.H. (1996a). Transport of cassiterite in a Malaysian stream: implications for geochemical exploration. Journal of Geochemical Exploration 57 (1996) 9-20.
19. Figueiredo, E.; Rodrigues,A.; Fonte, J.; Meunier, E.; Dias, F.;Lima, A.; Gonçalves, J.A.;Gonçalves-Seco, L.; Gonçalves, F.;Pereira, M.F.C. (2022). Tin and Bronze Production at the Outeiro de BaltarHillfort (NW Iberia). Minerals 2022,12, 758. https://doi.org/10.3390/M.
20. Gemmrich, L., Torró, L., Melgarejo, J.C., Laurent, O., Vallance, J., Chelle-Michou, C., Sempere, T.(2021). Trace element composition and U-Pb ages of cassiterite from the Bolivian tin belt. Mineralium Deposita,Spinger, 2021, 56 (8), pp.1491-1520. 10.1007/s00126-020-01030-3ff. hal-03436560
21. Girei, M.B., Huan, L., Thomas, J.A., Bonin, B., Ogunleye, P.O., Bute, S.I., Ahmed, H.A. (2019).Petrogenesis of A-type granites associated with Sn–Nb-Zn mineralization in Ririwai complex, north-Central Nigeria: Constraints from whole-rock Sm-Nd and zircon Lu-Hf isotope systematics. Lithos 340–341 49–70. https://doi.org/10.1016/j.lithos.2019.05.003.
22. Houketchang, B.M., Zhao, Y., Penaye, J., Zhang, S.H., Njel, U.O. (2015). Neoproterozoic subduction-related metavolcanic and metasedimentary rocks from the Rey Bouba Greenstone Belt of north-central Cameroon in the Central African Fold Belt: new insights into a continental arc geodynamic setting. Precambr. Res. 261, 40–53. https://doi.org/10.1016/j.precamres.2015.01.012
23. Houketchang, B.M., Penaye, J., Barbey, P., Toteu, S.F., Wandji, P. (2013). Petrology of high-pressure granulite facies metapelites and metabasites from Tchollire and Banyo regions: geodynamic implication for the Central African Fold Belt (CAFB) of north-central Cameroon. Precambrian Res. 224, 412–433.
24. Kankeu, B., Reinhard O. Greiling, R.O., Nzenti, J.P. (2009). Pan-African strike–slip tectonics in eastern Cameroon—Magnetic fabrics (AMS) and structure in the Lom basin and its gneissic basement. Precambrian Research174 (2009) 258–272.
25. Ketchaya, Y.B., Dong, G., Santosh, M., Lemdjou, Y.B. (2022). Microchemical signatures of placer gold grains from the Gamba district, northern Cameroon: Implications for possible bedrock sources. Ore Geology Reviews, 141 (2022) 104640.
26. Konopelko, D.L., Cherny, R.I., Petrova, S.V., Strekopytovd, S., Seltmannd, R., Vlasenko, N.S, Strekopytov,V.V., Mamadjanovg, Y.M., Wangh, X., Plotinskayai, S.Y., Andreeva, E.M. (2022). The Mushiston Sn deposit in Tajik Tien Shan as the type locality for stannite-cassiterite-hydrostannate mineralization: New mineral chemistry data and genetic constraints. Journal of Geochemical Exploration. Vol 239, 107017. https://doi.org/10.1016/j.gexplo.2022.107017.
27. Kouske, A.P., Suh, C.E., Ghogomu, R.T., Ngako, V. (2012). Na-Metasomatism and Uranium Mineralization during a Two-Stage Albitization at Kitongo, Northern Cameroon: structural and geochemical evidence. Int. J. Geosci. 03, 258–279. https://doi.org/10.4236/ijg.2012.31028
28. Lehmann,B. (2020). Formation of tin ore deposits: A reassessment, lithos, https://doi.org/10.1016/j.lithos.2020.105756.
29. Lerouge, C., Gloaguen, E., Wille, G., Bailly, L. (2017). Distributions of In and others rare-metals in cassiterite and associated mineral in Sn-+W ore deposits of the Western Variscan Belt. Eur. J. Mineral. 2017, 29, 739–753.
30. Li, X-H., Chen, Y., Tchouankoue, J.P., Liu, C.Z., Li, J., Ling, X.X., Tang, G.Q., Liu, Y. (2017). Improving geochronological framework of the Pan-African orogeny in Cameroon: New SIMS zircon and monazite UPb age constraints. Precambrian Research, v. 294, pp. 307–321.
31. Linnen, R.L., Van Lichtervelde, M.., & ˇCerný, P. (2012). Granitic pegmatites: Granitic pegmatites as sources of strategic metals. Elements 2012, 8, 275–280.
32. Linnen, R.L. (1998). Depth of emplacement, fluid provenance and metalllogeny in granitic terranes: a comparison of western Thailand with other tin belts. Min Deposita 33, 461–476.
33. Liorens, G,T., Moro, B.M.C., San, C.J.L., Lopez, M.F.J., Garcia, P., Fernandez , F.A. (2016). Tin-tantalum–niobium mineralization in the Penouta deposit (NW Spain : Textural features and and mineral chemistry to unravel the genesis and evolution of cassiterite and columbite group minerals in a peraluminous system. *Ore Geo. Rev. 2016, 81, 79-95*.

34. Makshakov, A.S., & Kravtsova, R.G. (2021).Stream Sediments of the Pestrinsk Ag-Au-Sn Bearing System (Northeastern Russia). Minerals 2021, 11, 65. https://doi.org/10.3390/ Min11010065.
35. Marjoribanks, R. (2010). Geological Methods in Mineral Exploration and Mining. Second Edition. Berlin Heidelberg: Springer-Verlag.
36. Meinhold, G., Andres, B., Kostopoulos, D. and Reischmann, T. (2008). Rutile Chemistry and Thermometry as Provenance Indicator: An Example from Chios Island, Greece. Sedimentary Geology, 203, 98-111. https://doi.org/10.1016/j.sedgeo.2007.11.004
37. Melcher, F., Graupner, T., Gabler, H.E., Sitnikova, M., Henjest-Hunst, F., Orberthur, T., Gerdes, A., Dewaele, S. (2015). Tantalum (niobium-tin) mineralization in Africa pegmatites and rare-meta granites. Constraints from Ta-Nb oxides mineralogy, geochemistry and U-Pb geochronology. Ore Geo. Rev. 64, 667-719.
38. Montes-Lauar., C.R., Trompette, R., Melfi,A.J., Bellieni,G., De Min,A., Peccerillio,E.M., Affaton,P., Pacca, I.J. (1997). Pan-African Rb-Sr isochron of magmatic rocks from northern Cameroon.Preliminary results. Brazil.pp204-205
39. Moles, N., & Chapman, R. (2011). Placer gold microchemistry in conjunction with mineralogy and mineral chemistry of heavy mineral concentrates to characterize bedrock sources. 25th International Applied Geochemistry Symposium 22-26 August 2011 Rovaniemi, Finland.
40. Murciego, A., Garcia Sanchez, A., Dusausoy, Y., Martin Pozas, J.M., Ruck, R.. (1997). Geochemistry and EPR of cassiterites from the Iberian Hercynian Massif. Mineral. Mag. 61, 357-365.
41. Neiva, A.M.R. (1996). Geochemistry of cassiterite and its inclusions and exsolution products from tin and tungsten deposits in Portugal. Can. Mineral. 34, 745-768
42. Ngako, V., Affaton, P., & Njonfang, E. (2008). Pan-African tectonics in northwestern Cameroon: Implication for the history of western Gondwana. Gondwana Res. 14, 509–522. https://doi.org/10.1016/j.gr.2008.02.002.
43. Ngako, V., Affaton, P., Nnange, J.M., Njanko, J.T. (2003). PanAfrican tectonic evolution in central and southern Cameroon: transpression and transtension during sinistral shear movements. Journal of African Earth Sciences, 36, 207–214.
44. Nguene, F. R. (1982). Geology and geochemistry of the Mayo Darle Tin deposit, West Central Cameroun central Africa, Ph.D. Thesis, New Mexico, Instit. of Min. and Techn. Socorro, New Mexico.
45. Neymark, L. A., Holm-Denoma, C. S., Larin, A. M., Moscati, R. J., Plotkina, Y.V. (2021). LA-ICPMS U-Pb dating reveals cassiterite inheritance in the Yazov granite, Eastern Siberia: Implications for tin mineralization. Mineralium Deposita https://doi.org/10.1007/s00126-020-01038-9.
46. Ngoniri, A. H., Djomo, H. D., Ngnotue, T., Kenne, P. A., Mbianya, G. N., Ganno, S., & Nzenti, J. P. (2021). Zircon Trace Element Geochemistry and Ti-in-Zircon Thermometry of the Ngazi-Tina Pan-African Post-Collisional Granitoids, Adamawa Cameroon. International Journal of Geosciences, 12, 307–328. https:// doi. org/ 10. 4236/ ijg. 2021. 124017.
47. Ngouabe, E.G.T., Vishiti, A., Nforba, M.T., Etame, R.S.J· Cheo Emmanuel Suh, C.E. (2022). Morphology and composition of alluvial gold from the Meiganga area, northern Cameroon: implications for provenance. Journal of Sedimentary Environments https://doi.org/10.1007/s43217-022-00115-5.
48. Omang, B.O., Che, V. B., Fon, A. N., Embui, V. F., Suh, C. E. (2014). Regional Geochemical Stream Survey For Gold Exploration in the Upper Lom Basin, Eastern Cameroon. International Journal of Geosciences, 5(9).Doi:10.4236/ijg.2014.59087.
49. Oyediran, I.A., Nzolang, C., Mupenge, M.P., Idakwo, S.O. (2020). Structural control and Sn-Ta-Nb mineralization potential of pegmatitic bodies in Numbi, South Kivu Eastern D.R Congo.
50. Pettke, T., Audétat, A., Schaltegger, U., and Heinrich, C. A. (2005). Magmatic-to-hydrothermal crystallization in the W-Sn mineralized Mole Granite (NSW,Australia) Part ?: evolving zircon and thorite trace element chemistry. Chem. Geol. 220, 191–213. doi: 10.1016/j.chemgeo.2005.02.017.
51. Rao, C., Wang, R.C., Hu, H., Zhang, W.L. (2015). Complex internal textures in oxide minerals from the Nanping No. 31 Dyke of Granitic Pegmatite, Fujian Province, Southeastern China. The Canadian Mineralogist. Vol. 47, pp. 1195-1212. DOI:10.3749/canmin.47.5.1195.
52. Seranti, S., Ferrini, V., Masi, U., Cabri, L.J. (2002). Trace-element distribution in cassiterite and sulfides from rubané and massive ores of the Corvo deposit, Portugal. The Canadian Mineralogist Vol. 40, 815-835.
53. Silva, M.M.V.G., Lopes, S.P., Gomesa, E.C. (2014). Geochemistry and behavior of REE in stream sediments close to an old Sn-W mined, Ribeira, northwestern Portugal. Chem.Erde Geochem, 74, 545-555.
54. Simons, B., Shail, R.K., Anderson, J.C.O. (2016). The petrogenesis of the early Permian Variscan granites of the Cornubian batholith: Lower plate post-collisional peraluminous magmatism in the Rhenohercynian Zone of SW England. *Lithos 260, 76-94.*
55. Sinclair, W.D., Gonevchuk, G.A., Korostelev, P.G., Semenyak, B.I., Rodionov, S.M., Seltmann, R., Stemprok, M., (2014). World tin and tungsten database. Geological survey of Canada.
56. Suh, C.E, Lehmann,B, Mafany,G.T. (2006). Geology and geochemical aspects of lode gold mineralized at Dimako-Mboscorro, S.E Cameroon , Geochem, Explor.Environ.Anal 6(4), 295-309.
57. Tchameni, R., Doumnang, J.C., Deudibaye, M., Branquet, Y. (2013). On the occurrence of gold mineralization in the Pala Neoproterozoic formations, South-Western Chad. J. Afr. Earth Sc. 84, 36–46. https://doi.org/10.1016/j.jafrearsci.2013.03.002.
58. Tchameni, R., Pouclet, A., Penaye, J., Ganwa, A.A., Toteu, S.F. (2006). Petrography and geochemistry of the Ngaoundéré Pan-African granitoids in Central North Cameroon: Implications for their sources and geological setting. J. Afr. Earth Sci. 44 (4–5), 511–529.
59. Tchunte, P.M.F., Tchameni, R, André-Mayer, A.S., Dakoure, H.S., Turlin, F., Poujol, M, Nomo, E.N., Fouotsa, A.S.F., Rouer, O. (2018). Evidence for Nb-Ta Occurrences in the Syn-Tectonic Pan-African Mayo Salah Leucogranite (Northern Cameroon): Constraints from Nb-Ta Oxide Mineralogy, Geochemistry and U-Pb LA-ICP-MS Geochronology on Columbite and Monazite. doi:10.3390/min8050188.

60. Toteu, S.F., Yongué F.R., Penaye J., Tchakounté, J., Mouangué,S.A.C., Schmus V.W.R., Deloule, E., Stendal, H. (2006). U-Pb dating of plutonic rocks involved in the nappe tectonic in southern Cameroon: consequence for the Pan-African fold belt. J Afr Earth Sci 44:479–493
61. Toteu, S.F., Penaye, J., & Djomani, Y.P. (2004). Geodynamic evolution of the Pan-African belt in central Africa with special reference to Cameroon. Can. J. Earth Sci. 41 (1), 73–85..**http://dx.doi.org/10.1139/e03-079.**
62. Toteu S.F., Van Schmus WR., Penaye J., Michard, A. (2001) New U–Pb and Sm–Nd data from north-central Cameroon and the pre-PanAfrican history of central Africa. Precambr Res 108:45–73.
63. Toteu, S.F. (1990). Geochemical characterization of the main petrographical and structural units of northern Cameroon, implication for panafrican evolution. Journal of African Earth Sciences, 10, 615-624. doi:10.1016/0899-5362(90)90028-D.
64. U.S. Geological Survey, (2020). Mineral commodity summaries 2020. https://pubs.usgs.gov/periodicals/ mcs2020/mcs2020.pdf. Accessed 19 Jun 2020.
65. Van Schmus, W.R., Oliveira, E.P., Da Silva Filho, A.F., Toteu, S.F., Penaye, J., Guimaraes, I.P. (2008). Proterozoic links between the Borborema Province, NE Brazil, and the Central African Fold Belt. Geol. Soc. London Spl Pub. 294 (1), 69–99.
66. Van Lichtervelde, M., Salvi, S., Beziat, D., Linnen, R.L. (2007). Textural features and chemical evolutionin tantalum oxides; magmatic versus hydrothermal origins for Ta mineralization in the Tanco lower pegmatite, Manitoba, Canada. Econ. Geol. 2007, 102, 257–276.
67. Woakes, M., Rahamant, M.A., & Aj1bade, A.C. (1987). Some metallogenetic features of the Nigerian Basement. Journal of African Earth Sciences. Vol. 6, No. 5, pp. 655-64.
68. Zack, S.M., & Gahtani, F.A. (2015). Provenance, diagenesis, tectonic setting and geochemistry of Hawksburg sandstone (Middle Triassic), southern Sdney basin, Australia. Turk.J.Earth. Sci. 24, 72-98.
69. Zhang R, Lu J., Lehmann B., Li, C., Li, G., Zhang, L., Guo, J., Sun, W. (2017). Combined zircon and cassiterite U–Pb dating of the Piaotang granite-related tungsten–tin deposit, southern Jiangxi tungsten district, China. Ore Geol Rev 82:268–284. https://doi.org/10.1016/j. oregeorev.2016.10.039.
70. Zhao, Y., Chen, S., Huang,Y., Zhao, J., Ton, X., Chen, X. (2019). U-Pb Ages, O Isotope Compositions, Raman Spectrum, and Geochemistry of Cassiterites from the Xi'ao Copper-Tin Polymetallic Deposit in Gejiu District, Yunnan Province. doi:10.3390/min9040212. www.altus strategies.com).

tables

Table 1. Electron microprobe analysis (EMPA) data for compositional variation of cassiterite grains of sample 1B from Mayo Darlé cassiterite deposit. All the analyses are reported in wt%

Sample/grain/point	1B/1/262	1B/1/263	1B/1/264	1B/1/265	1B/1/266	1B/1/267	1B/2/268	1B/2/269	1B/2/270	1B/2/271
SiO_2	0.367	0.345	0.293	0.332	0.345	0.315	0.349	0.322	0.334	0.318
CaO	0.715	0.694	0.729	0.726	0.711	0.71	0.694	0.756	0.697	0.705
FeO	0.336	0.504	0.394	0.699	0.248	0.22	0.277	0.287	0.498	0.823
SnO_2	99.694	97.897	98.145	98.301	99.262	99.678	98.613	98.995	97.064	99.019
MnO	0.008	0	0.003	0	0.014	0.003	0.016	0.032	0.033	0.012
Ta_2O_5	0.148	0.117	0.192	0.103	0.172	0.183	0.061	0.12	0.073	0.031
Total	101.268	99.557	99.756	100.161	100.752	101.109	100.01	100.512	98.699	100.908

Continuation of Table 1.

Sample/grain/point	1B/2/272	1B/2/273	1B/2/274	1B/2/275	1B/2/276	1B/2/277	1B/2/278	1B/3/279	1B/3/280	1B/3/281
SiO_2	0.3	0.352	0.337	0.295	0.312	0.378	0.309	0.301	0.302	0.287
CaO	0.691	0.697	0.731	0.721	0.731	0.694	0.69	0.727	0.722	0.711
FeO	0.541	0.19	0.299	0.519	0.807	0.586	0.533	0.263	0.363	0.306
SnO_2	99.223	98.01	98.713	98.895	98.937	98.759	98.749	99.178	97.831	99.254
MnO	0	0.017	0	0.021	0	0	0	0	0.019	0
Ta_2O_5	0.109	0.12	0.056	0.112	0.028	0.17	0.098	0.112	0.07	0.053
Total	100.864	99.386	100.136	100.563	100.815	100.587	100.379	100.581	99.307	100.611

Continuation of Table 1.

Sample/grain/point	1B/3/282	1B/3/283	1B/3/284	1B/3/285	1B/3/286	1B/3/287	1B/3/288	1B/3/289	1B/4/290	1B/4/291
SiO_2	0.321	0.316	0.389	0.338	0.35	0.355	0.292	0.3	0.361	0.315
CaO	0.716	0.72	0.702	0.714	0.848	0.735	0.704	0.696	0.725	0.708
FeO	0.285	0.47	0.775	0.325	0.855	0.228	1.091	0.332	0.582	0.711
SnO_2	98.657	98.374	98.498	97.703	97.844	99.147	98.206	99.153	98.839	98.777
MnO	0	0	0	0	0	0.015	0.002	0.027	0	0.024
Ta_2O_5	0.184	0.103	0.061	0.058	0	0.081	0.019	0.05	0.036	0.103
Total	100.163	99.983	100.425	99.138	99.897	100.561	100.314	100.558	100.543	100.638

Continuation of Table 1.

Sample/grain/point	1B/4/292	1B/4/293	1B/4/294	1B/4/295	1B/4/296	1B/5/297	1B/5/298	1B/5/299	1B/5/300	1B/5/301
SiO_2	0.372	0.361	0.331	0.316	0.348	0.357	0.368	0.287	0.347	0.329
CaO	0.721	0.715	0.729	0.721	0.695	0.731	0.704	0.692	0.737	0.724
FeO	0.528	0.288	0.727	0.225	0.532	0.031	0.814	0.282	0.443	0.246
SnO_2	99.061	98.111	98.535	99.566	98.637	98.488	98.177	97.626	99.328	99.252
MnO	0	0.022	0	0	0.048	0	0	0.014	0.019	0.031
Ta_2O_5	0.1	0.15	0.136	0.256	0.231	0.064	0.126	0.134	0.168	0.226
Total	100.782	99.647	100.458	101.084	100.491	99.671	100.189	99.035	101.042	100.808

Table 2. Electron microprobe analysis (EMPA) data for compositional variation of cassiterite grains of sample 2A from Mayo Darlé cassiterite deposit. All the analyses are reported in wt%.

Sample/grain/point	2A/1/155	2A/1/156	2A/1/157	2A/1/158	2A/1/159	2A/2/160	2A/2/161	2A/2/162	2A/2/163	2A/2/164
SiO_2	0.254	0.348	0.259	0.254	0.325	0.357	0.339	0.279	0.313	0.291
CaO	0.81	0.822	0.793	0.781	0.771	0.757	0.749	0.766	0.774	0.773
FeO	0.027	0.162	0.222	0.186	0.097	0.172	0.275	0.1	0.091	0.23
SnO_2	95.911	97.706	98.249	96.778	98.528	102.407	98.149	100.043	95.638	102.318
MnO	0.018	0.015	0	0.015	0	0.008	0	0.005	0.002	0.008
Ta_2O_5	0.058	0	0.077	0.254	0.08	0.098	0.081	0.092	0.101	0.12
Total	97.078	99.053	99.6	98.268	99.801	103.799	99.593	101.285	96.919	103.74

Continuation of Table 2.

Sample/grain/point	2A/2/165	2A/2/166	2A/3/167	2A/3/168	2A/3/179	2A/3/170	2A/3/171	2A/4/172	2A/4/173	2A/4/174
SiO_2	0.296	0.357	0.281	0.312	0.366	0.325	0.26	0.328	0.348	0.349
CaO	0.8	0.757	0.777	0.751	0.766	0.767	0.733	0.76	0.75	0.73
FeO	0.032	0.172	0.127	0.119	0.17	0.14	0.036	0.091	0.117	0.292
SnO_2	100.1	102.407	102.122	98.702	98.964	98.625	99.503	101.679	100.158	99.619
MnO	0	0.008	0	0	0	0.022	0	0.033	0.026	0.022
Ta_2O_5	0.12	0.098	0.114	0	0.092	0.184	0.156	0	0.067	0.095
Total	101.348	103.799	103.421	99.884	100.358	100.063	100.688	102.891	101.466	101.107

Continuation of Table 2.

Sample/grain/point	2A/4/175	2A/4/176	2A/4/177	2A/5/178	2A/5/179	2A/5/180	2A/5/181	2A/5/182
SiO_2	0.313	0.365	0.328	0.314	0.317	0.326	0.388	0.332
CaO	0.744	0.767	0.76	0.81	0.787	0.779	0.757	0.749
FeO	0.125	0.064	0.091	0.19	0.02	0.026	0.176	0.24
SnO_2	102.586	100.073	101.679	95.306	101.398	103.267	99.31	101.013
MnO	0.008	0	0.033	0.005	0.014	0.007	0	0.019
Ta_2O_5	0.181	0.131	0	0.117	0	0.089	0.128	0.075
Total	103.957	96.742	102.536	104.494	100.759	102.428	96.742	102.536

Table 3. Electron microprobe analysis (EMPA) data for compositional variation of cassiterite grains of sample 2B from Mayo Darlé cassiterite deposit. All the analyses are reported in wt%.

Sample/grain/point	2B/1/182	2B/1/183	2B/1/184	2B/1/185	2B/1/186	2B/1/187	2B/2/188	2B/2/189	2B/2/190	2B/2/191
SiO_2	0.297	0.28	0.274	0.296	0.348	0.337	0.336	0.257	0.312	0.236
CaO	0.781	0.717	0.737	0.749	0.783	0.749	0.733	0.745	0.766	0.764
FeO	0.018	0.175	0.411	0.16	0.144	0.107	0.182	0.346	0.002	0.272
SnO_2	99.446	95.709	96.865	100.221	98.669	98.838	100.813	97.564	100.479	99.233
MnO	0	0.017	0.008	0	0	0	0	0	0	0.007
Ta_2O_5	0.1	0.047	0.123	0.231	0.028	0.064	0.07	0.15	0.003	0.092
Total	100.642	96.945	98.418	101.657	99.972	100.095	102.134	99.062	101.562	100.604

Continuation of Table 3.

Sample/grain/point	2B/2/192	2B/2/193	2B/3/194	2B/3/195	2B/3/196	2B/3/197	2B/3/198	2B/4/199	2B/4/200	2B/4/201
SiO_2	0.305	0.28	0.357	0.316	0.322	0.341	0.288	0.254	0.286	0.354
CaO	0.761	0.742	0.79	0.768	0.783	0.765	0.781	0.759	0.759	0.768
FeO	0.016	0.085	0.044	0.053	0.161	0.055	0.005	0.169	0.033	0.019
SnO_2	102.039	98.308	99.728	100.607	97.738	91.913	95.208	96.241	99.099	99.885
MnO	0.034	0	0	0	0.023	0.014	0.025	0	0.039	0.033
Ta_2O_5	0.125	0.237	0.072	0.019	0	0.155	0.122	0.106	0.12	0.064
Total	103.28	99.652	100.991	101.763	99.027	93.243	96.429	97.529	100.336	101.123

Continuation of Table 3.

Sample/grain/point	2B/4/202	2B/4/203	2B/5/204	2B/5/205	2B/5/206	2B/5/207	2B/5/208
SiO_2	0.31	0.323	0.317	0.348	0.355	0.322	0.338
CaO	0.724	0.756	0.75	0.764	0.763	0.741	0.766
FeO	0.512	0.312	0.074	0.241	0.492	0.056	0.775
SnO_2	96.572	99.499	99.585	98.845	98.446	100.962	98.768
MnO	0	0	0	0.041	0	0.019	0
Ta_2O_5	0.179	0.165	0.145	0.188	0.027	0.08	0.113
Total	98.297	101.055	100.871	100.427	100.083	102.18	100.76

Table 4. Electron microprobe analysis (EMPA) data for compositional variation of cassiterite grains of sample 3A from Mayo Darlé cassiterite deposit. All the analyses are reported in wt%.

Sample/grain/point	3A/1/303	3A/1/304	3A/1/305	3A/1/306	3A/1/307	3A/1/308	3A/2/309	3A/2/310	3A/2/311	3A/2/312
SiO_2	0.3	0.256	0.299	0.364	0.346	0.36	0.359	0.266	0.288	0.337
CaO	0.719	0.724	0.709	0.708	0.721	0.724	0.681	0.701	0.704	0.696
FeO	0.157	0.186	0.41	0.122	0.13	0.113	0.317	0.484	0.237	0.108
SnO_2	96.74	98.125	97.395	97.848	98.199	97.549	96.363	98.086	97.696	96.864
MnO	0	0	0.002	0	0	0	0	0	0	0
Ta_2O_5	0.075	0.017	0.103	0.172	0.011	0.086	0.067	0.084	0.064	0.175
Total	97.991	99.308	98.918	99.214	99.407	98.832	97.787	99.621	98.989	98.18

Continuation of Table 4

Sample/grain/point	3A/2/313	3A/3/314	3A/3/315	3A/3/316	3A/3/317	2A/3/318	3A/4/319	3A/4/320	3A/4/321	3A/4/322
SiO_2	0.351	0.367	0.334	0.34	0.25	0.34	0.348	0.338	0.3	0.245
CaO	0.699	0.721	0.705	0.722	0.688	0.711	0.67	0.673	0.677	0.694
FeO	0.268	0.344	0.276	0.306	0.112	0.388	0.357	0.321	0.594	0.574
SnO_2	97.108	98.328	96.661	97.1	96.629	97.84	96.572	97.099	96.472	96.536
MnO	0.002	0	0	0	0.003	0	0	0	0.003	0
Ta_2O_5	0.072	0.061	0.228	0.014	0.086	0.094	0	0.159	0.242	0.095
Total	98.5	99.821	98.204	98.482	97.768	99.373	97.947	98.59	98.288	98.144

Table 5. Electron microprobe analysis (EMPA) data for compositional variation of cassiterite grains of sample 3B from Mayo Darlé cassiterite deposit. All the analyses are reported in wt%.

Sample/grain/point	3B/1/325	3B/1/326	3B/1/327	3B/1/328	3B/1/329	3B/1/330	3B/1/331	3B/1/332	3B/2/333	3B/2/334
SiO_2	0.303	0.331	0.339	0.301	0.303	0.32	0.346	0.328	0.325	0.238
CaO	0.691	0.712	0.707	0.677	0.675	0.679	0.67	0.676	0.681	0.707
FeO	0	0.177	0.024	0.678	0.799	0	0.087	0.671	0.279	0.091
SnO_2	96.159	96.953	95.809	95.518	95.965	95.643	93.849	94.674	94.005	95.618
MnO	0	0.019	0.015	0.042	0	0.028	0.028	0.021	0.015	0.008
Ta_2O_5	0.02	0.156	0.095	0.103	0.086	0.081	0.078	0.178	0.05	0.075
Total	97.173	98.348	96.989	97.319	97.828	96.751	95.058	96.548	95.355	96.737

Continuation of Table 5

Sample/grain/point	3B/2/335	3B/2/336	3B/2/337	3B/2/338	3B/2/339	3B/2/340	3B/2/341	3B/3/342	3B/3/343	3B/3/344
SiO_2	0.363	0.311	0.332	0.314	0.385	0.355	0.338	0.324	0.29	0.333
CaO	0.68	0.692	0.711	0.704	0.679	0.663	0.709	0.69	0.694	0.687
FeO	0.071	0.013	0.074	0.269	0.058	0.277	0.069	0.042	0.082	0.076
SnO_2	96.599	96.88	97.186	95.355	96.877	93.741	97.085	97.37	96.896	96.273
MnO	0.014	0.018	0	0.024	0.001	0	0.008	0	0.008	0.003
Ta_2O_5	0.086	0.178	0.058	0.145	0.092	0.064	0.059	0.162	0.011	0.092
Total	97.813	98.092	98.361	96.811	98.092	95.1	98.268	98.588	97.981	97.464

Continuation of Table 5

Sample/grain/point	3B/3/345	3B/3/346	3B/4/347	3B/4/348	3B/4/349	3B/4/350	3B/4/351	3B/5/352	3B/5/353	3B/5/354
SiO_2	0.304	0.313	0.32	0.32	0.307	0.273	0.285	0.322	0.335	0.281
CaO	0.689	0.729	0.709	0.741	0.708	0.707	0.689	0.699	0.707	0.683
FeO	0.275	0.014	0.185	0.008	0.014	0.014	0.386	0.947	0.057	0.004
SnO_2	95.036	97.061	96.831	96.557	96.771	97.573	95.703	96.627	97.828	97.678
MnO	0	0	0.018	0	0	0.04	0	0.028	0.01	0
Ta_2O_5	0.003	0	0.145	0.145	0.056	0	0.07	0.106	0.134	0.07
Total	96.307	98.117	98.208	97.771	97.856	98.607	97.133	98.729	99.071	98.716

Continuation of Table 5

Sample/grain/point	3B/5/355	3B/5/356	3B/5/357	3B/5/358
SiO_2	0.345	0.293	0.372	0.348
CaO	0.671	0.705	0.671	0.694
FeO	0.371	0	0.328	0.02
SnO_2	94.894	97.926	95.387	97.595
MnO	0.013	0.021	0	0
Ta_2O_5	0.184	0.064	0.178	0.173
Total	96.478	99.009	96.936	98.83

Table 6. Electron microprobe analysis (EMPA) data for compositional variation of cassiterite grains of sample 4A from Mayo Darlé cassiterite deposit. All the analyses are reported in wt%.

Sample/grain/point	4A/1/211	4A/1/212	4A/1/213	4A/1/214	4A/1/215	4A/2/216	4A/2/217	4A/2/218	4A/2/219	4A/2/220
SiO_2	0.246	0.346	0.315	0.294	0.307	0.345	0.344	0.297	0.289	0.404
CaO	0.705	0.724	0.694	0.697	0.688	0.726	0.691	0.685	0.715	0.696
FeO	0.574	0.022	0.597	0.109	0.103	0.077	0.114	0.084	0.123	0.351
SnO_2	97.508	97.724	97.91	97.974	98.016	97.805	98.075	98.126	97.984	96.264
MnO	0	0	0	0.007	0.004	0	0	0.009	0	0
Ta_2O_5	0.063	0.17	0.118	0.03	0.209	0.058	0.1	0.188	0.053	0.144
Total	99.096	98.986	99.634	99.111	99.327	99.011	99.324	99.389	99.164	97.859

Continuation of Table 6

Sample/grain/point	4A/3/221	4A/3/222	4A/3/223	4A/3/224	4A/3/225	4A/4/226	4A/4/227	4A/4/228	4A/4/229	4A/4/230
SiO_2	0.26	0.291	0.239	0.334	0.227	0.25	0.256	0.292	0.3	0.348
CaO	0.737	0.699	0.704	0.715	0.698	0.722	0.687	0.718	0.699	0.674
FeO	0.274	0.601	0.268	0.562	0.413	0.12	0.188	0.105	0.035	0.123
SnO_2	98.162	98.061	98.236	97.952	97.613	97.552	97.06	98.311	98.14	97.314
MnO	0.007	0	0	0.027	0	0.006	0	0.008	0	0
Ta_2O_5	0.056	0.114	0.125	0.256	0.058	0.175	0	0.081	0.211	0
Total	99.496	99.766	99.572	99.846	99.009	98.825	98.191	99.515	99.385	98.459

Continuation of Table 6

Sample/grain/point	4A/5/231	4A/5/232	4A/5/233	4A/5/234	4A/5/235
SiO_2	0.35	0.337	0.343	0.387	0.338
CaO	0.687	0.702	0.714	0.725	0.693
FeO	0.114	0.102	0.059	0.032	0.294
SnO_2	98.307	97.417	97.681	98.198	98.074
MnO	0.01	0	0	0.032	0
Ta_2O_5	0.014	0	0.12	0.006	0.05
Total	99.482	98.558	98.917	99.38	99.449

Table 7. Electron microprobe analysis (EMPA) data for compositional variation of cassiterite grains of sample 4B from Mayo Darlé cassiterite deposit. All the analyses are reported in wt%.

Sample/grain/point	4B/1/238	4B/1/239	4B/1/240	4B/1/241	4B/1/242	4B/2/243	4B/2/244	4B/2/245	4B/2/246	4B/2/247
SiO_2	0.327	0.311	0.31	0.315	0.312	0.343	0.336	0.319	0.368	0.303
CaO	0.707	0.708	0.701	0.722	0.715	0.713	0.693	0.73	0.715	0.747
FeO	0.462	0.21	0.492	0.089	0.288	0.038	0.099	0.049	0.121	0.087
SnO_2	99.631	99.644	99.724	100.332	99.811	102.869	100.106	100.04	98.934	99.416
MnO	0	0.03	0	0	0	0.014	0.019	0	0.027	0.026
Ta_2O_5	0.047	0.142	0.07	0.122	0.061	0.072	0.12	0.095	0.114	0.056
Total	101.174	101.045	101.297	101.58	101.187	104.049	101.373	101.233	100.279	100.635

Continuation of Table 7

Sample/grain/point	4B/3/248	4B/3/249	4B/3/250	4B/3/251	4B/3/252	4B/4/253	4B/4/254	4B/4/255	4B/4/256	4B/5/257
SiO_2	0.297	0.315	0.287	0.359	0.376	0.354	0.362	0.293	0.346	0.25
CaO	0.695	0.722	0.71	0.709	0.726	0.702	0.709	0.687	0.709	0.71
FeO	0.278	0.112	0.234	0.137	0.193	0.169	0.327	0.417	0.066	0.062
SnO_2	100.02	98.319	98.417	98.927	99.9	99.904	98.993	99.231	100.234	100.736
MnO	0.001	0	0	0.005	0	0	0	0	0	0
Ta_2O_5	0.125	0.122	0.047	0.047	0.072	0.042	0.103	0.045	0.111	0.1
Total	101.416	99.59	99.695	100.184	101.267	101.171	100.494	100.673	101.466	101.858

Continuation of Table 7

Sample/grain/point	4B/5/258	4B/5/259	4B/5/260	4B/5/261
SiO_2	0.344	0.38	0.353	0.332
CaO	0.701	0.706	0.676	0.749
FeO	0.062	0.291	0.235	0.1
SnO_2	98.903	98.689	95.82	100.504
MnO	0	0	0	0.021
Ta_2O_5	0.125	0.092	0.242	0.184
Total	100.135	100.158	97.326	101.89

Table 8. Electron microprobe analysis (EMPA) data for compositional variation of cassiterite grains of sample 5A from Mayo Darlé cassiterite deposit. All the analyses are reported in wt%.

Sample/grain/point	5A/1/261	5A/1/262	5A/1/263	5A/1/264	5A/1/265	5A/1/266	5A/1/267	5A/1/268	5A/1/269	5A/1/270
SiO_2	0.33	0.313	0.335	0.338	0.29	0.358	0.328	0.361	0.254	0.338
CaO	0.706	0.66	0.704	0.683	0.688	0.735	0.706	0.699	0.721	0.682
FeO	0.29	0.305	0.349	0.661	0.232	0.256	0.461	0.706	0.532	0.223
SnO_2	98.485	98.296	98.948	97.981	99.217	98.218	97.401	97.304	99.299	98.235
MnO	0.046	0	0	0	0.028	0	0	0	0	0
Ta_2O_5	0.17	0.159	0.064	0.256	0.064	0.008	0.011	0.014	0.12	0.095
Total	100.027	99.733	100.4	99.919	100.519	99.575	98.907	99.084	100.926	99.573

Continuation of Table 8

Sample/grain/point	5A/2//271	5A/2/272	5A/2/273	5A/2/274	5A/2/275	5A/2/276	5A/2/277	5A/2/278	5A/3/279	5A/3/280
SiO_2	0.3	0.278	0.405	0.365	0.349	0.321	0.345	0.315	0.406	0.361
CaO	0.695	0.723	0.739	0.697	0.682	0.715	0.678	0.705	0.716	0.709
FeO	0.207	1.185	0.804	1.222	1.231	0.949	0.9	0.702	1.228	0.248
SnO_2	97.876	98.627	97.818	99.773	97.05	97.477	98.147	99.008	97.341	98.76
MnO	0.015	0.047	0	0	0.056	0	0	0	0.008	0
Ta_2O_5	0.022	0.05	0	0.075	0.014	0.042	0.106	0.137	0.212	0
Total	99.115	100.91	99.766	102.132	99.382	99.504	100.176	100.867	99.911	100.078

Continuation of Table 8

Sample/grain/point	5A/3/281	5A/3/282	5A/3/283	5A/3/284	5A/3/285	5A/3/286	5A/3/287	5A/3/288	A5/4/289	5A/4/290
SiO_2	0.353	0.288	0.416	0.354	0.332	0.292	0.309	0.345	0.361	0.315
CaO	0.698	0.696	0.718	0.698	0.731	0.716	0.694	0.692	0.701	0.7
FeO	0.302	0.198	0.605	0	0.327	0.386	1.302	0.513	0.384	0.69
SnO_2	99.606	99.805	98.97	98.768	99.476	99.77	97.911	98.109	98.609	98.28
MnO	0	0.02	0	0	0.02	0.007	0	0.015	0.044	0
Ta_2O_5	0.177	0.116	0	0.158	0	0.108	0.078	0.097	0.067	0.075
Total	101.136	101.123	100.709	99.978	100.886	101.279	100.294	99.771	100.166	100.06

Continuation of Table 8

Sample/grain/point	5A/4/291	5A/4/292	5A/4/293	5A/4/294	5A/4/295	5A/4/296	5A/4/297	5A/4/298
SiO_2	0.327	0.247	0.334	0.377	0.282	0.437	0.322	0.35
CaO	0.712	0.704	0.732	0.73	0.695	0.731	0.689	0.72
FeO	0.306	0.326	0.256	0.52	0.069	0.168	0.658	0.249
SnO_2	99.091	98.999	98.853	98.296	100.178	99.581	99.418	98.515
MnO	0.021	0.017	0.006	0.018	0.009	0.018	0.018	0.011
Ta_2O_5	0.153	0.137	0.109	0	0.084	0.067	0.028	0.198
Total	100.61	100.43	100.29	99.941	101.317	101.002	101.133	100.043

Table 9. Electron microprobe analysis (EMPA) data for compositional variation of cassiterite grains of sample 5B from Mayo Darlé cassiterite deposit. All the analyses are reported in wt%.

Sample/grain/point	5B/1/361	5B/1/362	5B/1/363	5B/1/364	5B/1/365	5B/2/366	5B/2/367	5B/2/368	5B/2/369	5B/2/370
SiO_2	0.315	0.288	0.344	0.276	0.313	0.335	0.318	0.312	0.309	0.333
CaO	0.796	0.781	0.786	0.794	0.774	0.812	0.817	0.804	0.804	0.83
FeO	0.408	0.677	0.22	0.235	0.203	0.342	0.392	0.086	0.866	1.069
SnO_2	96.326	99.473	97.42	97.365	99.519	99.778	97.071	98.843	95.672	98.136
MnO	0.009	0.007	0	0.004	0	0	0.009	0	0	0
Ta_2O_5	0.12	0.086	0	0.072	0.003	0.097	0	0.061	0.053	0
Total	97.974	101.312	98.77	98.746	100.812	101.364	98.607	100.106	97.704	100.368

Continuation of Table 9

Sample/grain/point	5B/2//371	5B/3/372	5B/3/373	5B/3/374	5B/2/375	5B/3/376	5B/4/377	5B/4/378	5B/4/379	5B/4/280
SiO_2	0.29	0.296	0.269	0.302	0.318	0.352	0.307	0.296	0.282	0.304
CaO	0.804	0.794	0.827	0.807	0.824	0.848	0.799	0.828	0.798	0.799
FeO	1.062	1.385	0.365	0.855	1.547	0.202	1.067	0.096	0.269	0.188
SnO_2	96.932	99.934	99.793	95.489	98.196	97.671	101.084	101.375	100.105	96.272
MnO	0.004	0.051	0	0.01	0	0.012	0	0.001	0	0
Ta_2O_5	0.047	0.047	0.017	0.1	0.092	0.039	0.084	0.092	0.164	0.011
Total	99.139	102.507	101.271	97.563	100.977	99.124	103.341	102.688	101.618	97.574

Continuation of Table 9

Sample/grain/point	5B/4/281	5B/4/282	5B/5/383	5B/5/384	5B/5/385	5B/5/386	5B/5/587
SiO_2	0.276	0.292	0.336	0.299	0.325	0.312	0.336
CaO	0.803	0.835	0.814	0.809	0.778	0.822	0.788
FeO	0.911	0.32	0.933	0.862	0.949	0.135	1.084
SnO_2	101.242	103.8	100.099	99.929	99.804	100.722	100.11
MnO	0	0.007	0	0.029	0.015	0	0.001
Ta_2O_5	0.086	0.103	0.212	0.059	0.153	0.106	0.036
Total	103.318	105.357	102.394	101.987	102.024	102.097	102.355

Figures

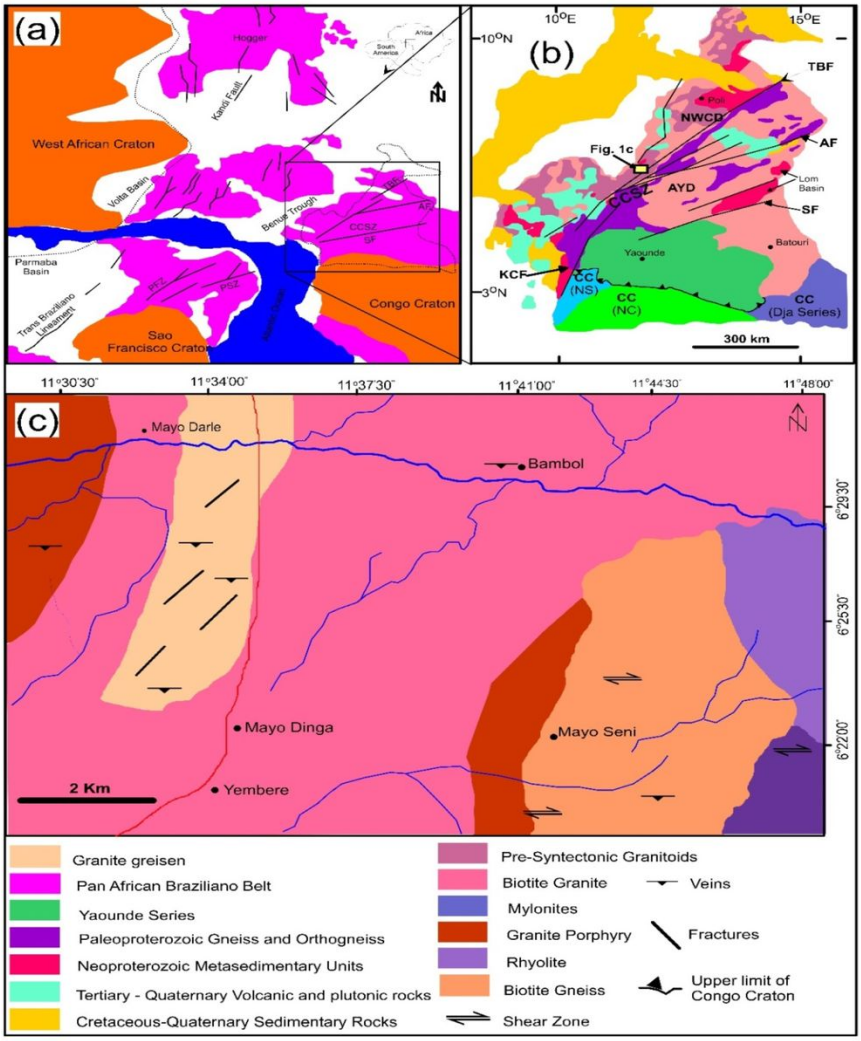

Figure 1

Geological setting of the study area. (**a**) Pre-drift reconstruction of the Pan-African/Braziliano shear zones between São Francisco, Congo and West African Cratons (modified fromVan Schmus et al., 2008), (**b**) Geologic map of Cameroon showing the main lithostratigraphic domains of the Neoproterozoic Pan-African orogenic belt, (adapted from Toteu et al., 2001), (**c**) Geologic map of the Mayo Darlé region .TBF: Tcholliré-Banyo fault, AF: Adamaoua Fault, CCSZ: Central Cameroon Shear Zone, SF: Sanaga Fault, YD:Yaounde Domain, AYD: Adamaoua Yade Domain, NWCD: North western Cameroon Domain, PF:Patos Fault , PSZ: Pernambuco Shear Zone.

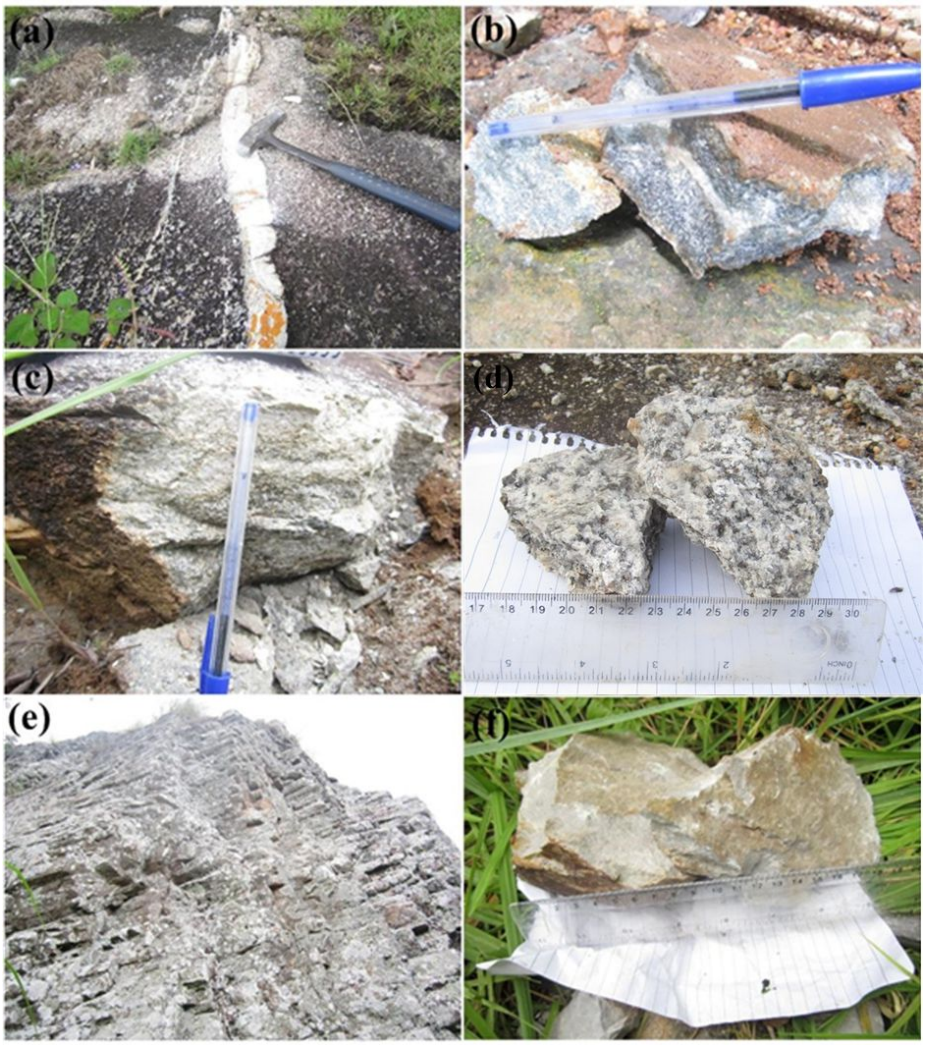

Figure 2

Field photographs and hands specimen **(a-b)** Biotite gneiss outcrop occurring as slab with crosscutting quartz-veins and hands specimen with sporadic or weak foliation, **(c-d)** Biotite granite outcrop and hands specimen, **(e)** blocky rhyolite outcrop with columnar joints, **(f)** very fine-grained, grey rhyolite hand specimen.

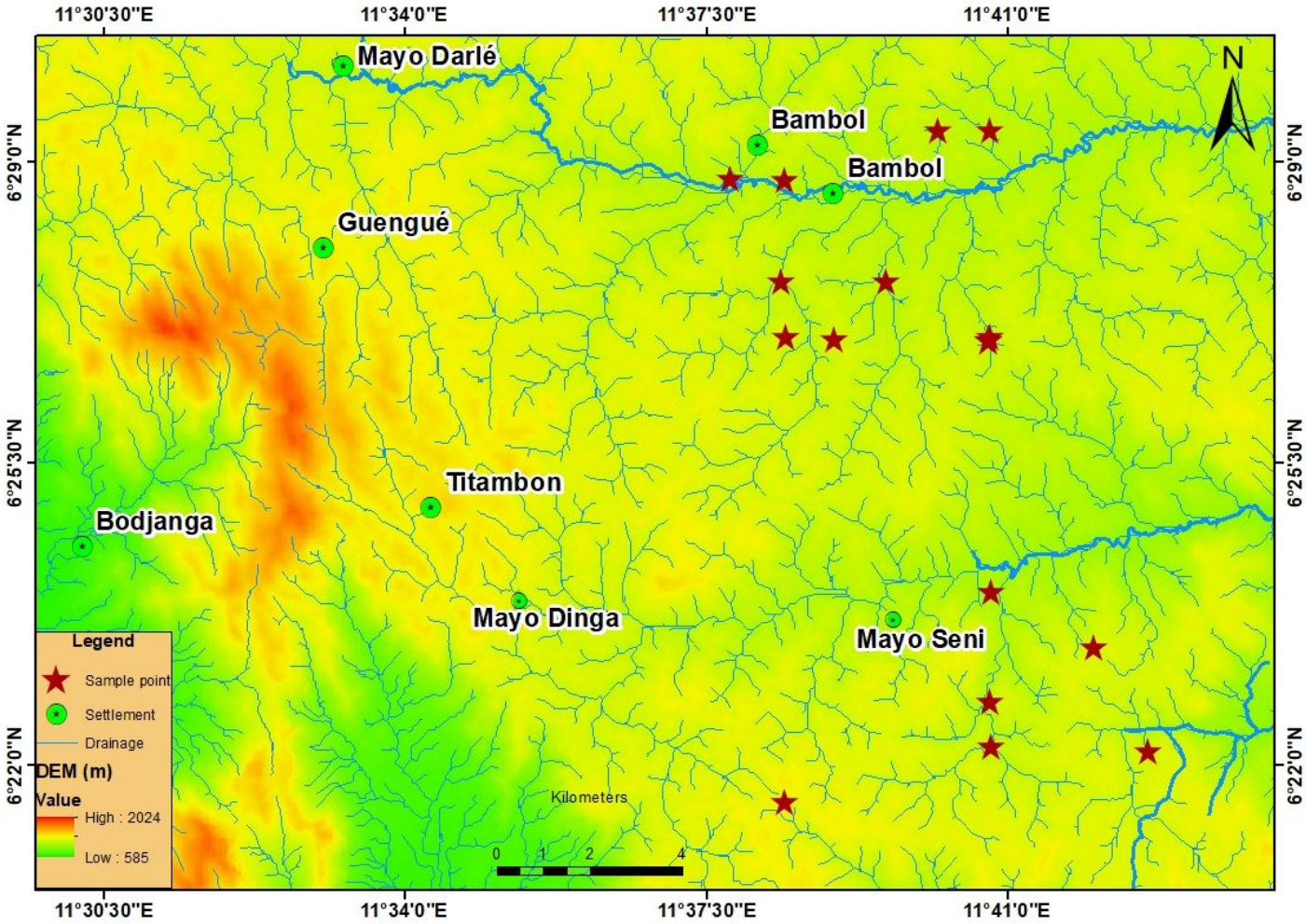

Figure 3

Drainage map of the Mayo Darléregion, showing the sample location points.

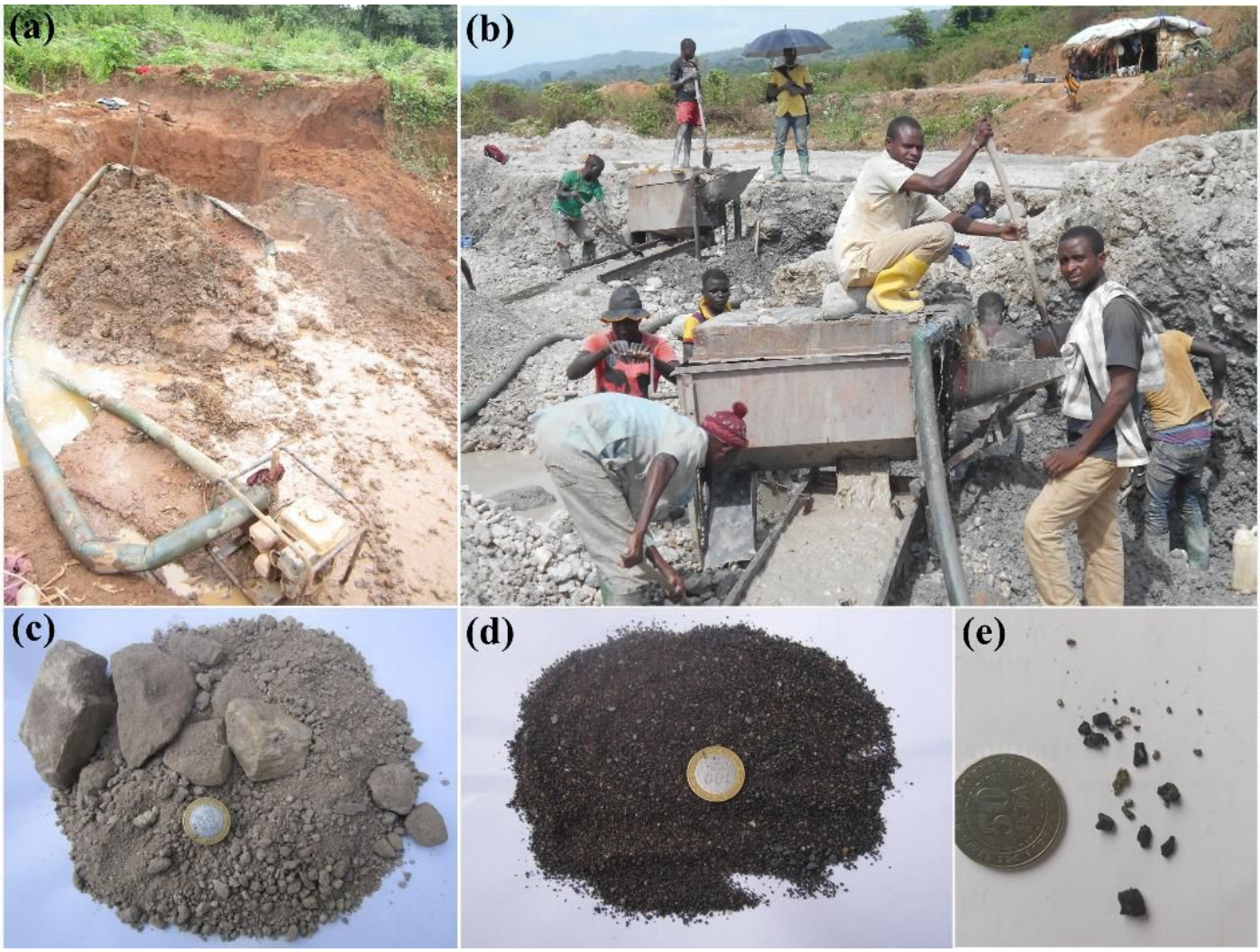

Figure 4

Alluvial mining activities in the Mayo Darlé region (a-b) artisanal miners using sluicing boxes and panning techniques to recover alluvial cassiterite concentrates from pitted conglomeratic beds materials (c) conglomeratic beds materials (d) cassiterite concentrates (e) cassiterite grains.

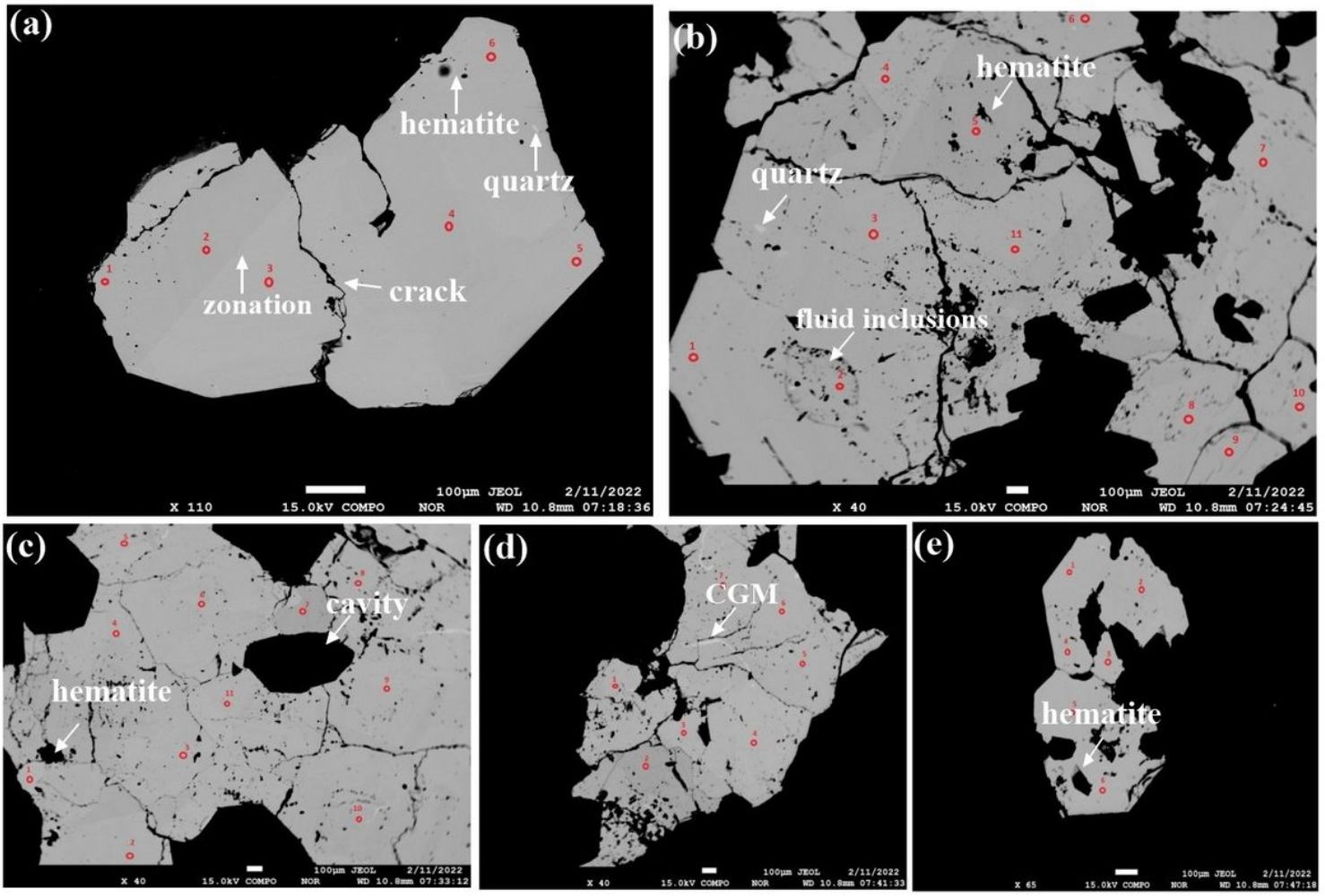

Figure 5

Sample 1B BSE images of cassiterite (a) angular grain with a smooth texture, zonation and hematite inclusions, (b-d) grains with rough surface textures, hematite, columbite group minerals (CGM) and quartz mineral inclusions.

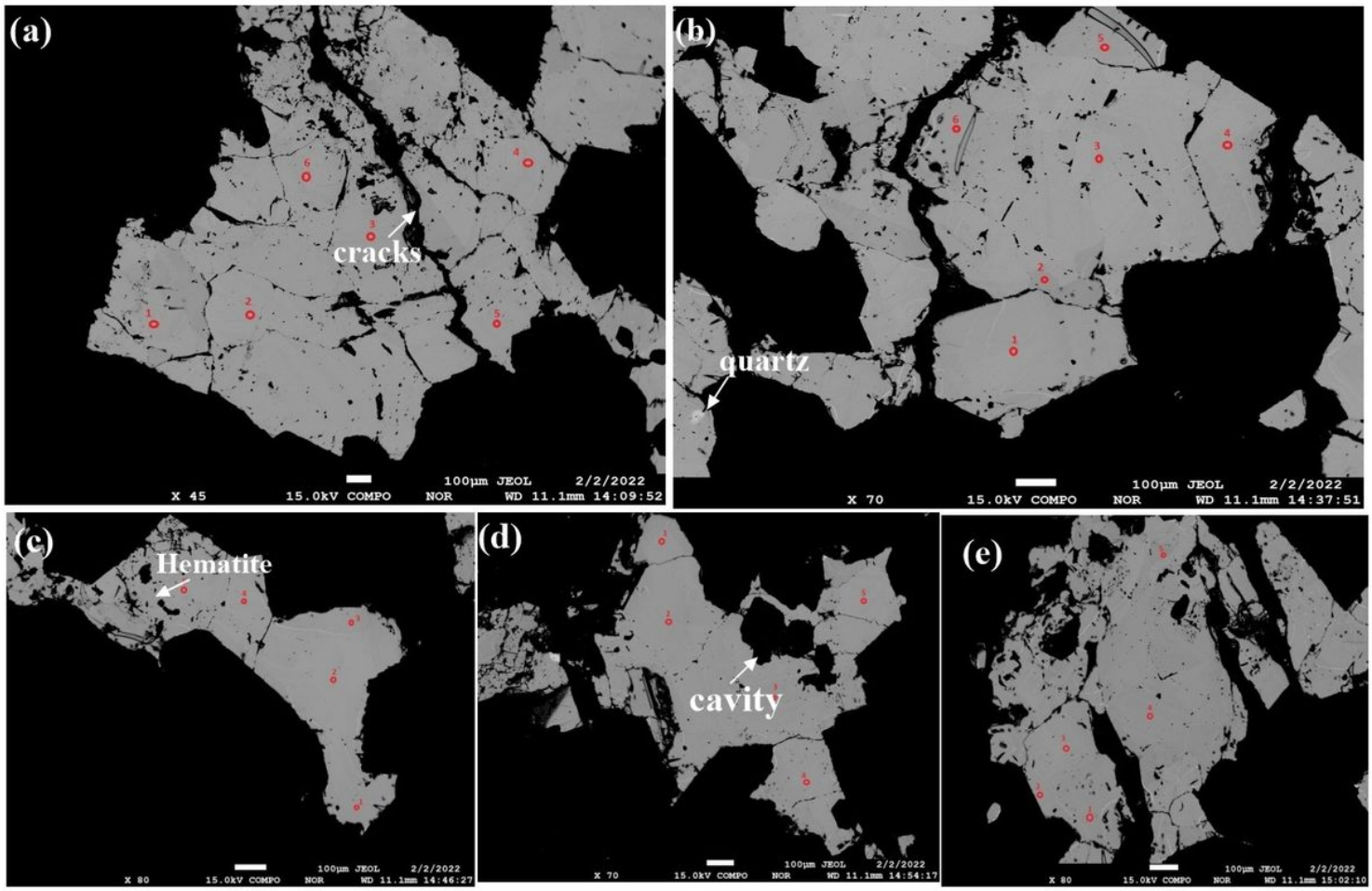

Figure 6

Sample 2A BSE images of cassiterite (a-d) sub-angular to elongated grains with rough/irregular surface textures, with embedded hematite, columbite group minerals (CGM) and quartz mineral inclusions.

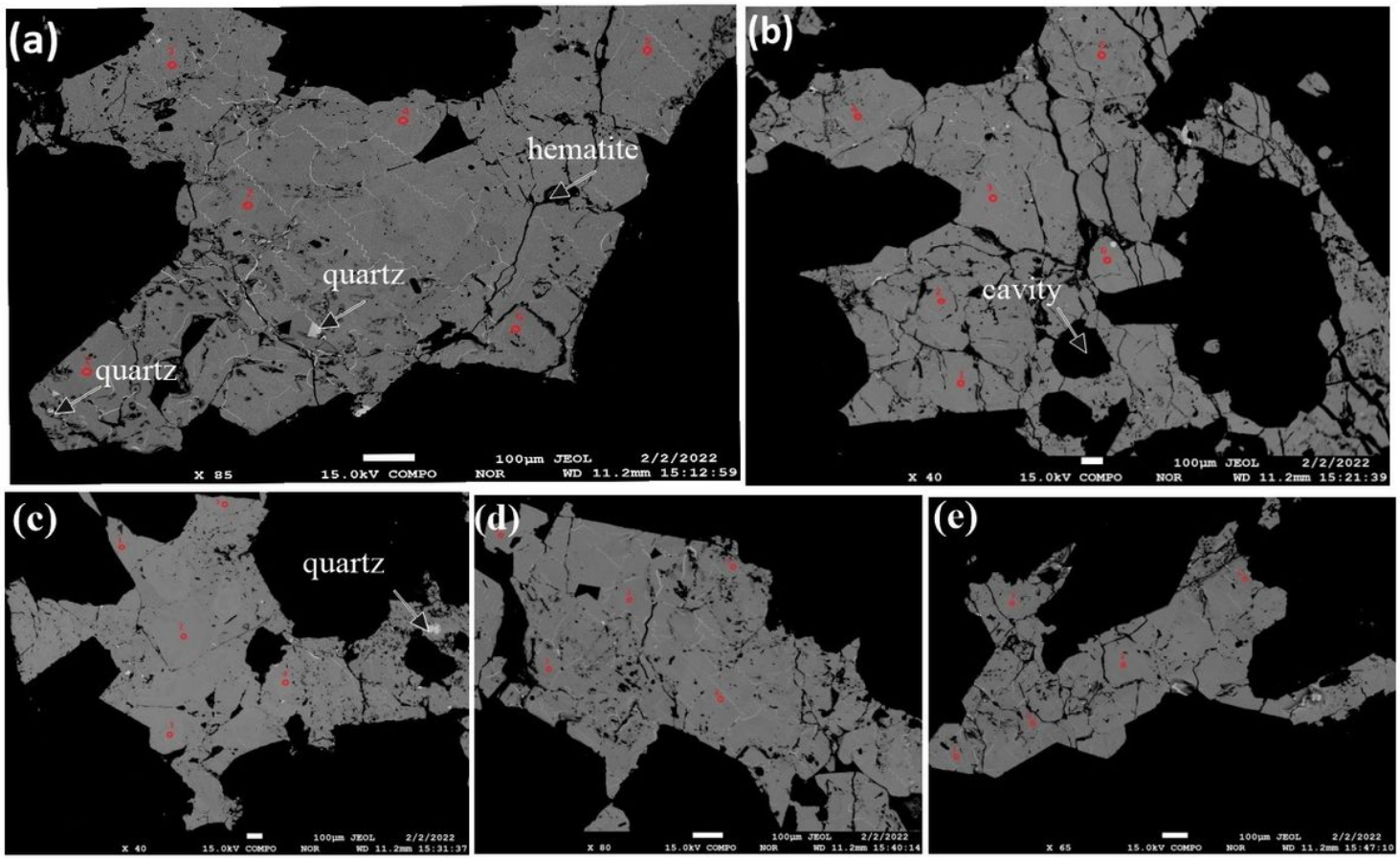

Figure 7

Sample 2B BSE images of cassiterite (a-d) elongated grains with rough/irregular surface textures, with embedded hematite, columbite group minerals (CGM) and quartz mineral inclusions.

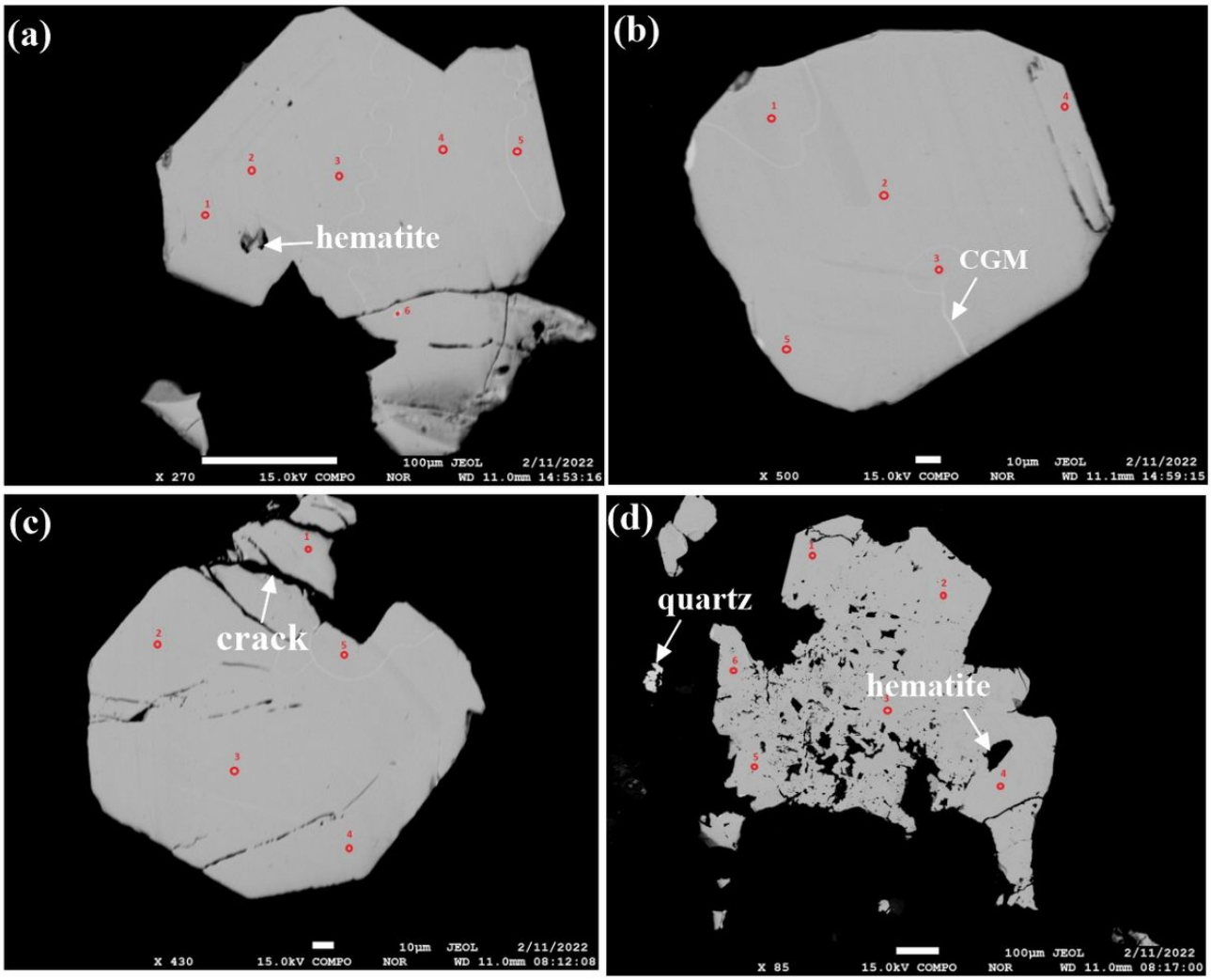

Figure 8

Sample 3A BSE images of cassiterite (a-c) sub-rounded to rounded grains with smooth/regular surface textures, (d) sub-angular grain withrough/irregular surface texture, with embedded hematite, columbite group minerals (CGM) and quartz mineral inclusions.

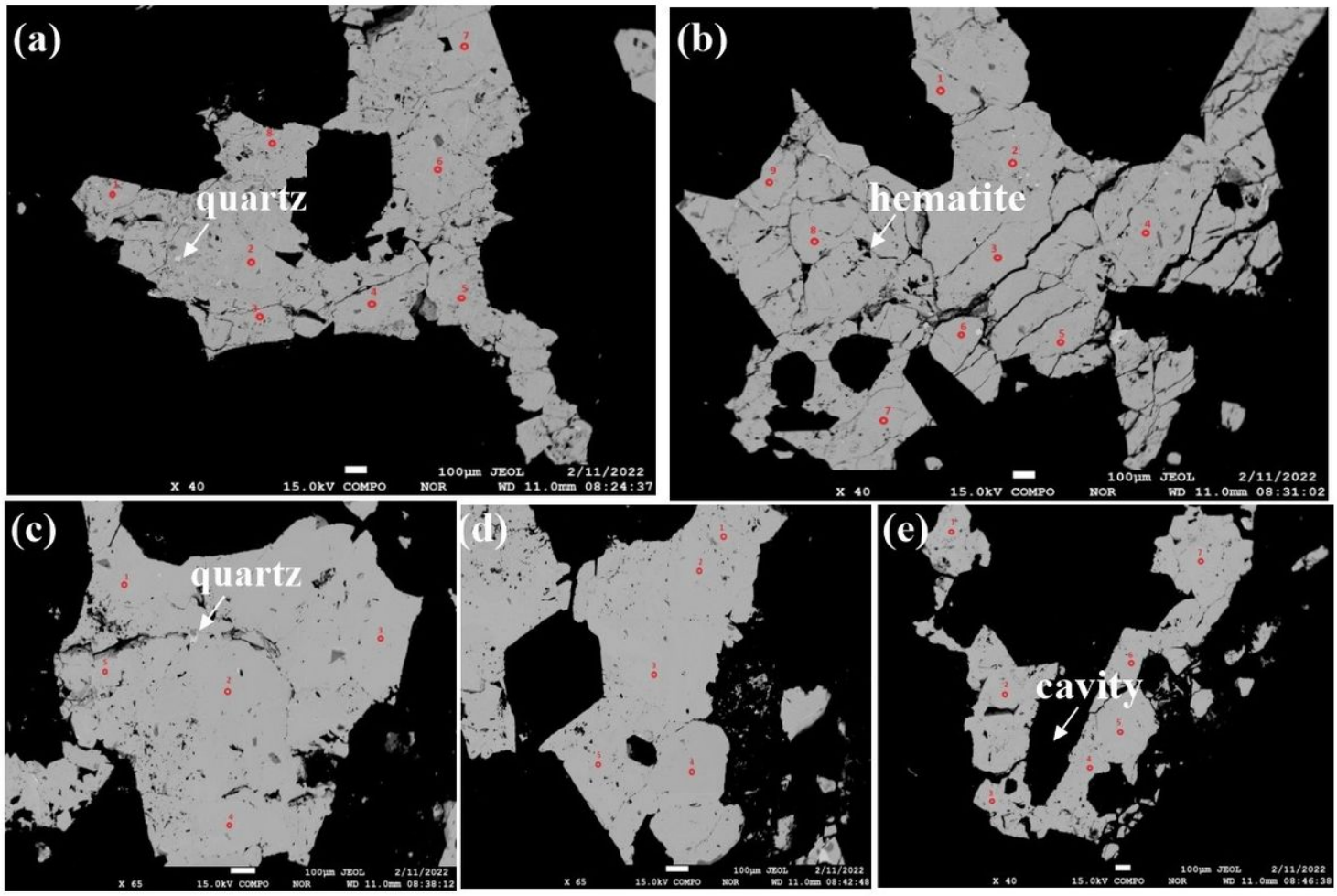

Figure 9

Sample 3B BSE images of cassiterite, (a, b, d, e) irregular grains with microtextures (quartz, hematite and cavities), (c) angular grains.

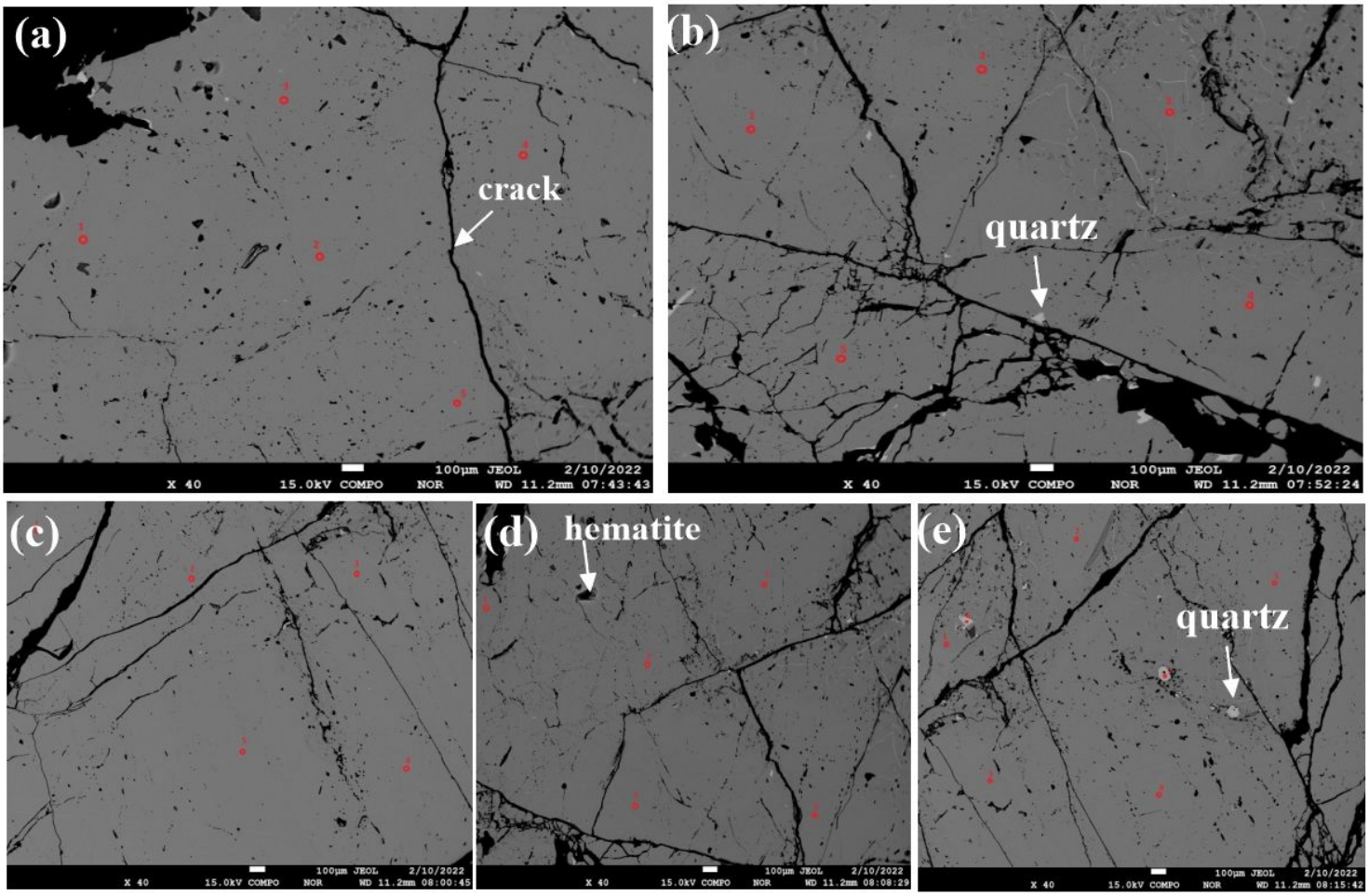

Figure 10

Sample 4A BSE images of cassiterite (a-e) grains withrough/irregular surface textures, with embedded hematite and quartz mineral inclusions.

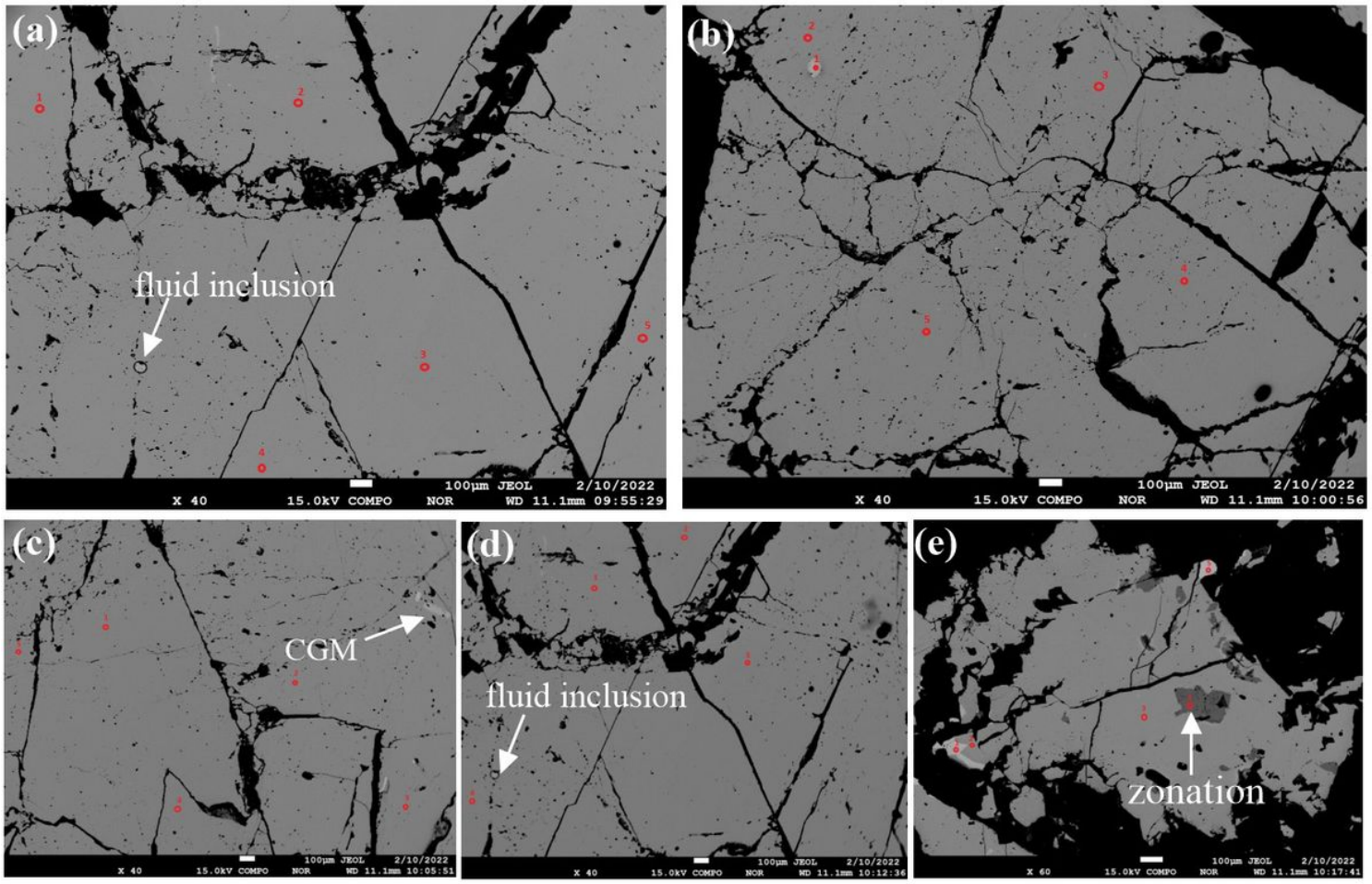

Figure 11

Sample 4B BSE images of cassiterite (a-e) grains with rough/irregular surface textures, with cavities, cracks, and hematite, quartz, CGM and fluids inclusions as microtextures.

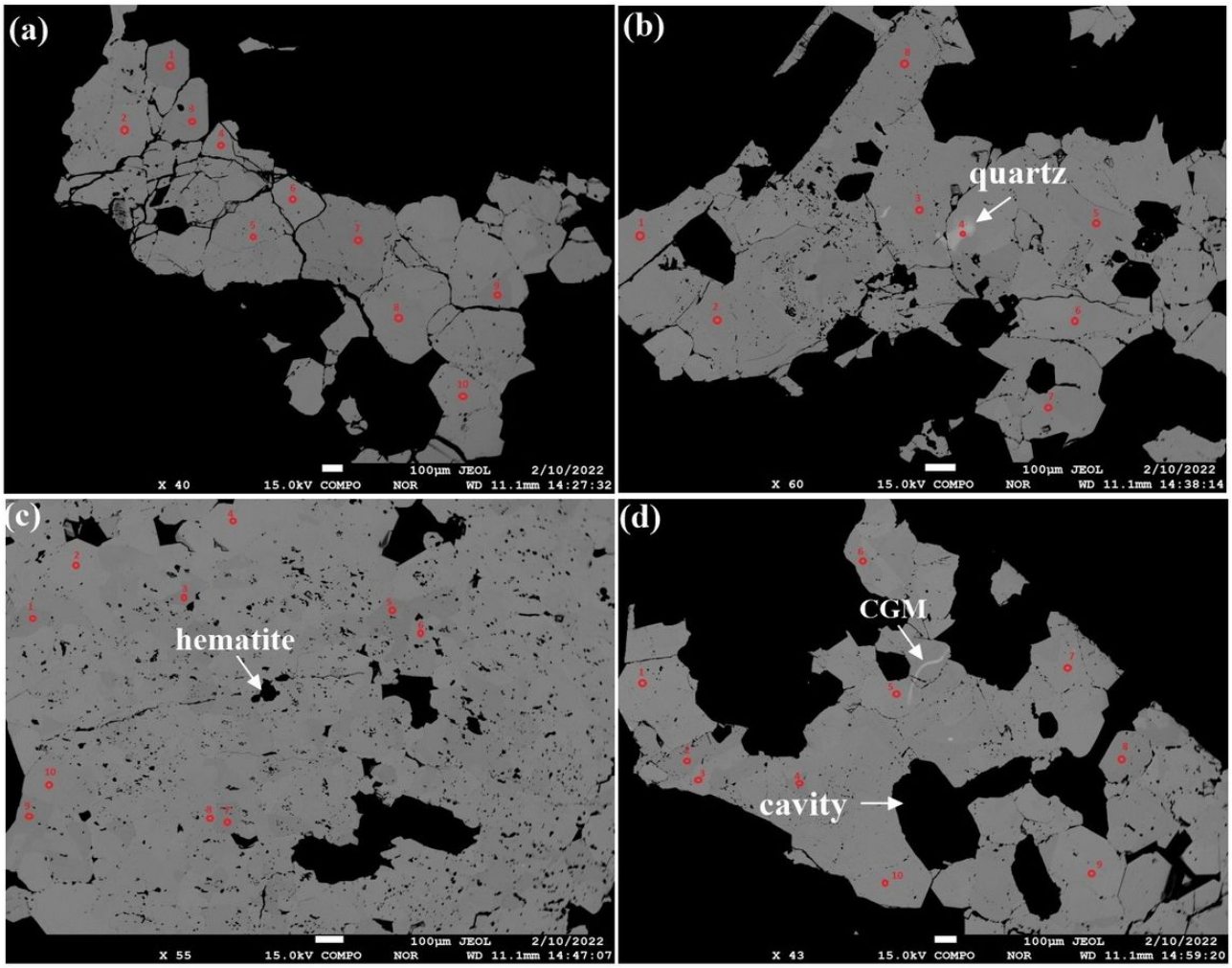

Figure 12

Sample 5A BSE images of cassiterite (a-d) elongated grains with rough/irregular surface textures, with embedded hematite, columbite group minerals (CGM) and quartz mineral inclusions. Cavities are common.

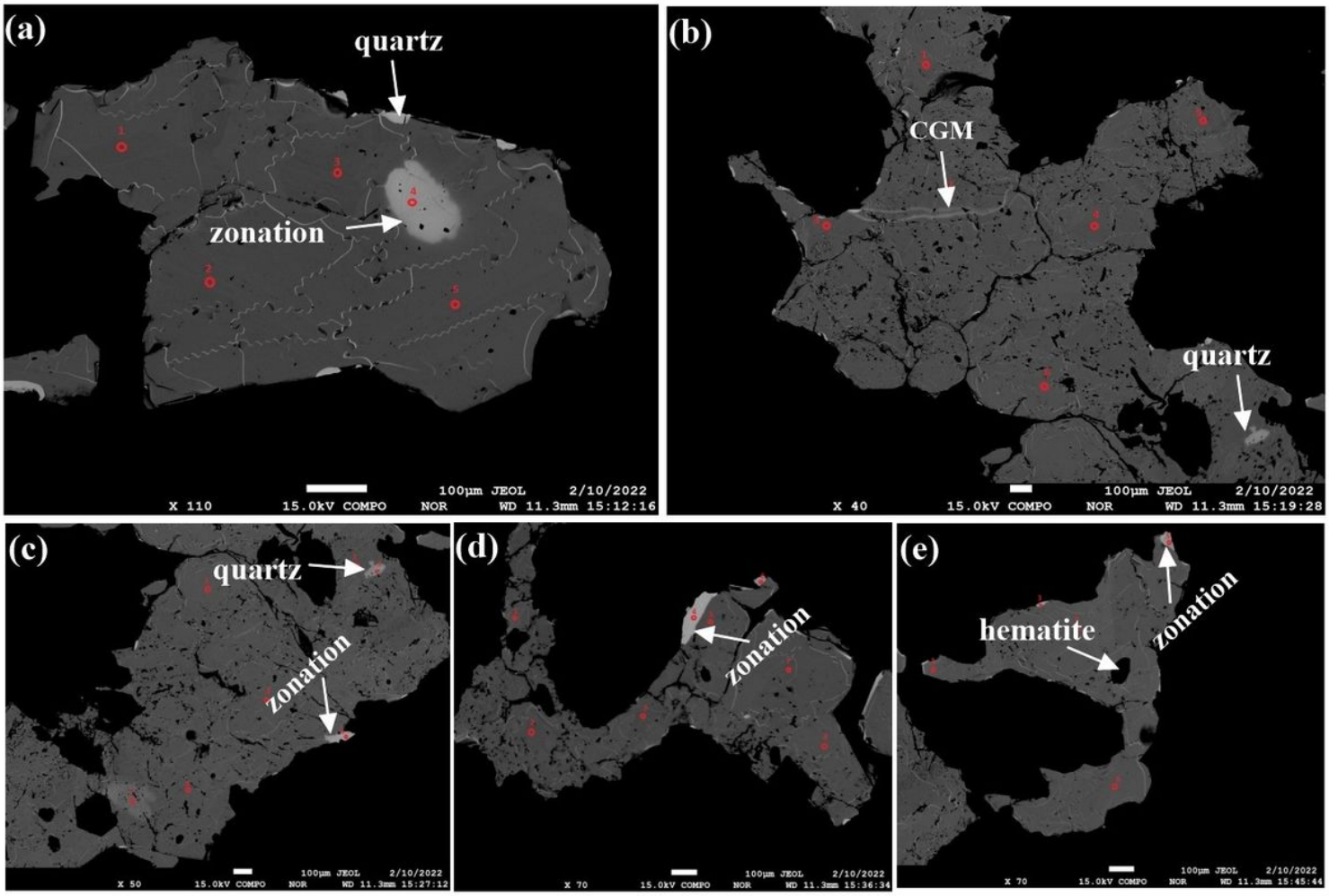

Figure 13

Sample 5B BSE images of cassiterite (a-e) irregular grains with quartz, hematite and CGM inclusions, with zonations respectively.

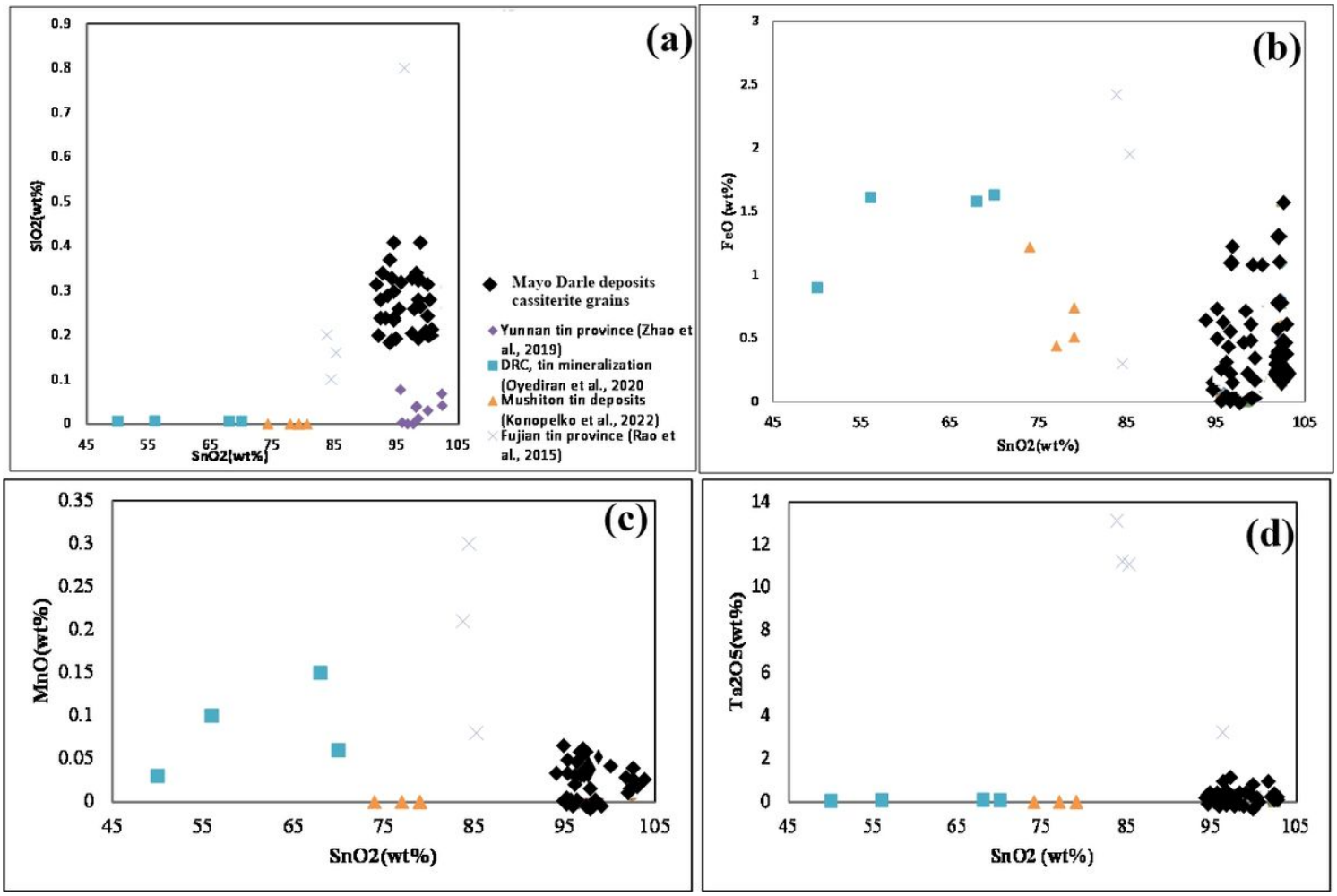

Figure 14

(a-d) Compositional plots of Si, Fe, Mn,Ta and Sn oxides showing variation of Mayo Darlé deposit samples (1B, 2A, 2B, 3A, 3B, 4A, 4B, 5A and 5B) with other cassiterite deposits in the world (Zhao et al. 2019; Oyediran et al. 2020; Konopelko et al.2022;Rao et al.2015).

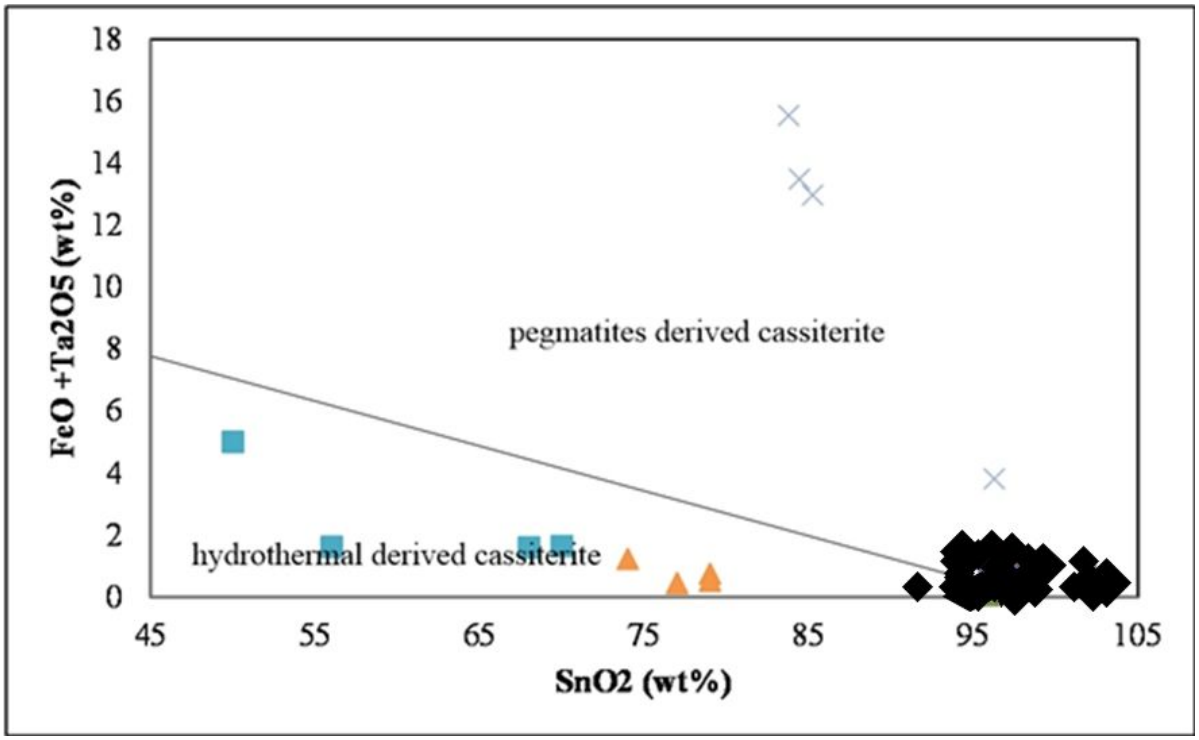

Figure 15

Compositional variations plot of cassiterite samples from the Mayo Darlé region deposits , Gejiu tin District, Yunnan Province (Zhao et al., 2019), DRC tin mineralization (Oyediran et al., 2020), Mushiton tin deposits (Konopelko et al., 2022) and Fujian tin province (Rao et al., 2015). (Plot adapted from Moles and Chapman., 2011). Same symbols as in fig. 14.